Imaging air volume fraction in sea ice using non-destructive X-ray tomography

O. Crabeck[1], R.J. Galley[1], B. Delille[2], B.G.T. Else[3], N.-X. Geilfus[4], M.Lemes[1], M. Des Roches[5], , P.Francus[5], J.-L. Tison[6] and S. Rysgaard[1,4,7]

[1] {Department of Geological Sciences, Centre for Earth Observation, University of Manitoba, Winnipeg, Manitoba, Canada}

[2] {Unité d'Océanographie Chimique, MARE, Université de Liège, Liège, Belgium}

[3] {Department of Geography, University of Calgary, Calgary, Alberta, Canada}

[4] {Arctic Research Centre, Aarhus University, Aarhus, Denmark}

[5] {Centre Eau terre et Environement, INRS-Été-Quebec, Quebec, Canada}

[6] {Laboratoire de Glaciologie, DSTE, Université Libre de Bruxelles, Bruxelles, Belgium}

[7] {Greenland Climate Research Centre, Greenland Institute of Natural Resources, Nuuk, Greenland}

Correspondence to: O.Crabeck (crabecko@myumanitoba.ca)

Abstract

Although the presence of a gas phase in sea ice creates the potential for gas exchange with the atmosphere, the distribution of gas bubbles and transport of gases within the sea ice are still poorly understood. Currently no straightforward technique exists to measure the vertical distribution of air volume fraction in sea ice. Here, we present a new fast and non-destructive X-ray computed tomography technique to quantify the air volume fraction and produce separate images of air-volume inclusions in sea ice. The technique was performed on relatively thin (4 −22 cm) sea ice collected from an experimental ice tank. While most of the internal layers showed air-volume fractions <2%, the ice-air interface (top 2 cm) systematically showed values up to 5%. We suggest that the air volume fraction is a function of both the bulk ice gas saturation factor and the brine volume fraction. We differentiate micro bubbles ($\emptyset < 1$ mm), large bubbles ($1 < \emptyset < 5$ mm) and macro bubbles ($\emptyset > 5$mm). While micro bubbles were the most abundant type of air inclusions, most of the air porosity observed resulted from the presence of large and macro bubbles. The ice texture (granular and columnar) as well as the permeability state of ice are important factors controlling the air volume fraction. The technique developed is suited for studies related to gas transport and bubble migration.

1 Introduction

Sea ice is a multi-phase system consisting of ice crystals, salt precipitates, brine, and gas bubbles (i.e. air inclusions). The abundance and morphology of brine and air inclusions are strongly dependent on the temperature and salinity of the sea ice (Cox and Weeks, 1983; Weeks and Ackley, 1986). Microscale studies of sea ice inclusions have in large part focused on the formation and morphology of brine inclusions (as pockets and/ or channels) (e.g. Bennington, 1967; Bock and Eicken, 2005; Cole and Shapiro, 1998; Cox and Weeks, 1975; Eicken et al., 2000; Eide and Martin, 1975; Galley et al., 2015a; Hunter et al., 2009; Notz and Worster, 2008). Inclusions in large part control the transfer of heat, salt, gases, and radiation between the ocean and atmosphere (Light et al., 2003). Brine and air inclusions in sea ice also affect the optical and electromagnetic properties of sea ice, and are often sites of biological activity (Fritsen et al., 1994, Krembs et al., 2000; Vancoppenolle et al., 2014).

Studies on the formation and morphology of gas inclusions and gas transport within sea ice are sparse. The air porosity quantitatively defined by the air volume fraction (V_a %) has generally been neglected in past work; it has long been assumed that gas species in sea ice were dissolved in brine and subject to the same processes as brine inclusions, and that the air volume fraction is minor compared to the brine volume fraction. Mushy layer theory, whose equations are now used as the physical basis for liquid exchange processes within sea ice neglect the presence of air inclusions (Feltham et al., 2006; Worster, 1992; Worster, 1997; Rees Jones and Worster, 2013). Omission of air inclusions in sea ice research propagates a lack of understanding of gas transport within sea ice, though studies in the last decade have revealed substantial CO_2 fluxes at the sea ice-atmosphere interface (Semiletov et al., 2004; Zemmelink et al., 2006; Delille et al., 20014; Geilfus et al., 2014, 2015; Normura et al., 2006; 2010; 2013). It was also recently argued that a major part of the natural gases (oxygen, nitrogen and argon) as well as methane (CH_4) reside in the gas phase inside bubbles in sea ice rather than dissolved in the brine (Zhou et al., 2013; Moreau et al., 2014; Crabeck et al., 2014a, b). Therefore the physical properties and processes of air inclusions in sea ice can potentially control the sea ice–atmosphere exchange of gases. The most important process leading to the formation of air inclusions from entrapped brine is brine volume reduction by freezing (Zhou et al., 2013; Crabeck et al., 2014a, b; Moreau et al., 2014). Increasing brine salinity during winter due to sea ice temperature reduction results in reduced gas solubility causing super-saturation (the *brine concentration effect*), which leads to bubble formation if

66　the sum of the partial pressures of all the dissolved gases is higher than the local hydrostatic

67　pressure.

68

69　Previous studies of air inclusions morphology in sea ice were based on horizontal thin

70　sections (e.g., Grenfell, 1983; Perovich and Gow, 1991, 1996; Light et al., 2003; Cole et al.,

71　2004). Grenfell, (1983), Perovich and Gow, (1996) and Cole et al., (2004) highlighted that the

72　columnar ice is usually depleted in air inclusions while top granular ice is described as bubbly

73　with larger air inclusions. Grenfell (1983) measured bubble number distributions in small

74　samples cut from first year sea ice, observing diameters ranging from 0.2 to 4 mm. Perovich

75　and Gow (1996) reported mean bubble diameters ranging from 0.036 mm to 0.56 mm for 30

76　cm thick pancake ice and mean diameter of 2.6 mm on a multi-year hummock. Light et al.,

77　(2003) recorded 100 images from thin sections in transmitted light and reported bubble

78　diameters between 0.008 mm to 0.14 mm in ice columnar ice that was 175 cm thick (Light et

79　al., 2003).

80　　　　Limitations of current methods have resulted in a lack of details on determination of

81　air volume fraction. Those methods provide inadequate profiles of the vertical distribution of

82　air inclusions in sea ice, especially in the context of ocean-sea ice-atmosphere exchange of

83　gas. The sea ice air-volume fraction is most often determined empirically from bulk

84　temperature, salinity and density measurements (after Cox and Weeks, 1983).　However,

85　small errors associated with sea ice density measurements result in large errors in the

86　calculated air-volume fraction.　Perovich and Gow (1996), and Light et al. (2003) used sea ice

87　sections imaged using transmitted light to describe air inclusions within sea ice, given the

88　caveats that undisturbed microstructure required careful thermal control, size may be limited,

89　and the distinction between gas and brine can be ambiguous in transmitted images. While thin

90　section studies are relevant to detail morphometric analysis of inclusions, profile of air

91　volume fraction cannot be deduced from thin section analysis. Another approach is high

92　resolution measurements of the total gas content along a vertical profile using techniques

93　initially developed for continental ice cores (melting-refreezing and toepler pump extraction

94　or summing individual gases concentrations measured using gas chromatography (GC) (Tison

95　et al., 2002)). These techniques however operate under vacuum, and therefore collect both the

96　dissolved and gaseous phases. Also, this technique does not provide information on the

97　morphology of the bubble content. A third approach used previously is to melt the ice sample

98　in a gas tight container and quantify total gas volume (Rysgaard and Glud, 2004). A problem

99　with this approach, however, is that gases equilibrate to a new bulk gas concentration

depending on the salinity and temperature of the melting ice and hence do not represent the actual gas volume at *in situ* conditions.

We propose a methodological advancement employing computed tomography (CT) X-ray imaging for measurement of air inclusions within sea ice. For many years CT X-ray has been widely used as a medical diagnostic tool. This non-invasive technique has largely contributed to the study of rock fractures and rock porosity, and has recently been applied to the sea ice field, advancing percolation theory for the brine system (Golden et al., 2007; Pringle et al., 2009, Obbard et al., 2009). Here we present high-resolution profiles of the distribution of air inclusions in sea ice, which are derived from CT X-ray images of whole ice cores at the sub-millimeter scale. A detailed statistical analysis of the air volume fraction in experimental sea ice is presented, as well as comparisons to the air volume equations of Cox and Weeks (1983) and measurement of total gas content. Throughout this work, we highlight the parameters and processes influencing the air porosity (air volume fraction, V_a).

2   Methods

2.1   Sea ice Environmental Research Facility (SERF)

The Sea-ice Environmental Research Facility (SERF) at the University of Manitoba (Winnipeg, Canada) is an in-ground concrete pool with dimensions of 23.3 m (length) x 9.2 m (width) x 2.75 m (depth). It is filled each year with seawater formulated on site to closely replicate the chemistry of Arctic surface seawater (e.g. Hare et al., 2013, Geilfus et al., 2013, Rysgaard et al., 2014). In January 2013 an experiment was initiated from open water conditions, where sea ice was allowed to grow to 22 cm thick between January 13 and January 26. Ice cores were collected on January 14, 16 and 25 to measure bulk ice gas composition, temperature, salinity, and density, and for computed tomography (CT) X-ray imaging.

2.2   Sea ice core: temperature, salinity and texture

At least four ice cores were extracted on each sampling occasion using a Mark II core barrel with an internal diameter of 9 cm (Kovacs Ent., Lebanon NH, USA). One of the cores was destructively interrogated to measure an in situ ice temperature profile at a depth resolution of 2 cm using a calibrated probe (Testo 720, precision ± 0.1°C) inserted into pre-drilled holes perpendicular to the ice core depth axis. The second ice core extracted was immediately cut into 2 cm slices which were stored in polyethylene buckets and left to melt close to 0°C. Bulk ice salinity of the melt of these 2-cm sections was derived from sample

132 conductivity and temperature measured with an Orion Star Series WP-84TP conductivity

133 meter (precision ± 0.1) using the equations of Grasshoff et al. (1983). For sea ice gas content

134 and CT X-ray imaging, the third and fourth cores were immediately wrapped in polyethylene

135 bags and stored at -20°C in the dark to ensure brine/gas immobilization and to inhibit

136 biological processes (Eicken, 1991).

2.3 Gas composition

138 The bulk ice concentration of argon (Ar), oxygen (O_2) and nitrogen (N_2) expressed in

139 μ mol L^{-1} ice were analyzed using gas chromatography (GC). The dry-crushing technique as

140 developed for gas measurements in continental ice (e.g. Raynaud et al., 1982) was used to

141 extract the gas phase from the sea ice samples in a cold laboratory at -25°C. Each ice core

142 sample for gas composition was cut in 5-cm sections, and 60 g of each section were put into a

143 vessel together with stainless steel beads which was evacuated to 10^{-3} torr, and then fixed to

144 an ice crusher (after Raynaud et al., 1982 and Stefels et al., 2012). The stainless steel beads

145 impact the ice block during the shaking process, crushing it into a fine powder. After

146 crushing, the vessel was kept in a cold ethanol bath (-50°C) and connected to a gas

147 chromatograph (Trace GC) equipped with a thermal conductivity detector for concentration

148 analyses (Skoog et al., 1997). We used AlphagazTM2 He (Air Liquid –P0252) as the carrier

149 gas and a 22 ml packed column (Mole Sieve 5A 80/100; 5 m x 1/8"). Gas collected included

150 both gas bubbles in the ice and from the dissolved phase within the brine, which cannot be

151 differentiated using this method. The total gas content (ml L^{-1} ice) was derived from the sum

152 of the O_2, N_2 and Ar concentrations initially expressed in μ mol L^{-1} ice and applying the

153 perfect gas law. Since both the cutting process and evacuation stage during the measurement

154 process lead to potential gas lost, the total gas content measured is a minimum estimate of the

155 true total gas content.

156 The saturation level of a gas affects bubble nucleation in brine inclusions and is

157 therefore a crucial parameter determining gas flux at the ice-air interface. Theoretically,

158 nucleation occurs when the sum of the partial pressures of dissolved gases is higher than the

159 local hydrostatic pressure. We therefore compared (i) the gas concentrations profile measured

160 in bulk ice; $C_{bulk\ ice}$ to (ii) the theoretical inventory predicted by the solubility in brine at

161 atmospheric saturation; $C_{Saturation}$ (i.e. the maximum concentration of O_2, N_2 and Ar in the

162 dissolved phase when the brine is not supersaturated (Carte, 1961; Lubetkin, 2003; Zhou et

163 al., 2013)). $C_{Saturation}$ is obtained by calculating the temperature and salinity-dependent

164 solubility of O_2, N_2 and Ar in the brine (Garcia and Gordon, 1992; Hamme and Emerson,

165 2004) and multiplying it by the relative brine volume (i.e. the brine volume fraction (V_b), see
166 below) and expressed in ml L^{-1} of bulk ice. These relationships are valid for the range of
167 temperature and salinity found in sea ice (Zhou et al., 2013). It is important to note that C_{bulk}
168 $_{ice}$ is measured on 5 cm ice sections while $C_{saturation}$ is computed using 2 cm sections, we can
169 compute more than one $C_{saturation}$ value for each $C_{bulk\ ice.}$ The ratio between the gas
170 concentration measured ($C_{bulk\ ice}$) and the air concentration at equilibrium ($C_{saturation}$) gives the
171 saturation factor SAT_f. As a result, we present the mean SAT_f and its standard deviation for
172 each $C_{bulk\ ice}$ (5 cm) section. When a strong gradient of temperature, salinity, and therefore
173 brine volume occurs in a $C_{bulk\ ice}$ 5 cm section, the standard deviation of SAT_f increases.

2.4 Bulk ice density and Air volume Fraction

175 To compute the brine volume fraction and the air volume fraction, the bulk ice density
176 of 5-cm core sections was measured with the Mass-Volume technique in a cold lab (-20°C)
177 and the Cox and Weeks (1983) equations were then employed. Ice core sections were cut into
178 cubes of 5 cm^3 and weighed precisely to determine their mass (M). The dimensions of the
179 sample were measured giving their volume (V). The density of the ice (ρ_i) calculated by:

$$\rho_i = \frac{M}{V} \qquad (1)$$

181 This common technique is easily applied, but there are several possible sources of
182 errors: obtaining a dimensionally perfect ice sample is difficult, and inaccuracies in the
183 measurement of the sample dimensions lead to volume error (Timco and Frederking, 1995).
184 To limit error induced by imperfect sample dimensions, we used a precision diamond wire
185 saw. The length of each edge (the number of edges per cube = 12) was found to deviate from
186 5 cm by ± 0.07 cm on average (total number of edges measured = 96; 8 ice cubes) yielding an
187 average precision for ice density of ±4.4%, as a result of the cutting process. While deviation
188 of 0.7 mm on the dimension of the ice cube has little effect on the precision of the density and
189 of the calculated brine volume fraction (relative standard error <5%), it produces relative
190 standard errors as high as 163% on the air volume fraction computed using the equations of
191 Cox and Weeks (1983) (Table 1).

2.5 Liquid porosity: brine volume fraction

193 The brine volume was calculated according to Cox and Weeks (1983) using in situ
194 temperature, bulk ice salinity, and bulk ice density measurements from the cores. Brine
195 salinity (S_b) was calculated using in situ sea ice temperatures and the freezing point of
196 seawater (UNESCO, 1978). The brine volume fraction, (V_b, expressed in %), was calculated

197   from the ratio of brine volume and bulk sea ice volume (b/V). In previous works, sea ice air

198   volume fraction is ubiquitously neglected, so historically, sea ice porosity refers solely to the

199   brine volume fraction. In the context of this paper, the terms brine inclusions and brine

200   volume fraction refers to liquid porosity. The permeability threshold of $V_b = 5\%$ following

201   Golden et al (1998, 2007) defines permeable and impermeable columnar sea ice.

2.6 Ice texture:

203   To describe the ice crystal texture, horizontal thin sections of maximum 10 cm length

204   were produced in a cold lab at -20°C using the standard microtome (Leica SM2400)

205   procedure described by Langway (1958) and Tison et al. (2008). Images of these backlit

206   horizontal thin sections were taken in the cold lab between crossed polarizing sheets with a

207   camera (Nikon Coolpix S200).

2.7 Air porosity: air volume fraction by CT X-ray imaging:

2.7.1 General principle

210   CT scanning is a non-destructive radiographic approach to examine materials by

211   creating a three-dimensional image of density contrasts. Ice cores were imaged using a third

212   generation Siemens Somatom Volume Access sliding gantry medical CT-Scanner (Siemens

213   SOMATOM Definition AS+ 128) at the Institut National de la Recherche Scientifique (INRS-

214   ETE). The ice cores were stored at -20°C and scanned at room temperature. The scan duration

215   was less than 15 seconds. Including transport of the ice samples from the storage freezer to

216   the CT instrument was less than 75 seconds. We therefore assume that no temperature change

217   in the core occurred. Data was acquired in spiral mode with a pitch factor of 0.6; the X-ray

218   source was set at 120kV and 150 mAs. These configurations produced 1152 projections for

219   each reconstructed axial slice. The image size is limited by the manufacturer to 512 x 512

220   pixels, so the pixel resolution is defined by the chosen field of view (FOV). The smallest

221   selectable FOV is 50 x 50mm providing a pixel resolution of 0.0977 mm in the transverse

222   plane. This FOV is too small to contain the whole core in one image; so four reconstructions

223   of each core were produced and concatenated together using Matlab. The Siemens SAFIRE

224   (Sinogram Affirmed Iterative Reconstruction) reconstruction algorithm was used (three

225   iterations). The convolution kernel is J70h, a medium-sharp filter. The final image size was

226   1024 x 1024 pixels with a pixel resolution of 0.0977 mm (x-y) and a slice thickness (z) of 0.6

227   mm. By scanning a core from top to bottom, a three-dimensional "stack" of images was

228   produced by compiling individual transverse slices and longitudinal slices (Fig. 1a) yielding

229      $0.097 \times 0.097 \times 0.6$ mm (0.0056 mm^3) voxel volumes within square (1024 x 1024 voxel)

230   images.

231   Hounsfield (1973) and Knoll (1989) describe the X-ray technique in detail. The

232   Hounsfield Unit (HU) value for each voxel corresponds to linear X-ray attenuation (Duliu,

233   1999), where higher density and higher atomic numbers result in greater X-ray attenuation.

234   Ice core density was calculated in terms of tomographical intensity (TI) (in Hounsfield Units

235   for each voxel):

236
$$TI = \left(\frac{\mu}{\mu_w} - 1 \right) * 1000 \qquad (2)$$

237   Where μ is the linear absorption coefficient of the bulk core, and μ_w is the linear absorption

238   coefficient of water. μ is a function of the radiation energy and the atomic number of the

239   core component crossed by the beam and varies in relation to the density of the material.

240   Resulting images are represented in grey scale where darker tones indicate lower density

241   material (e.g. air) (Fig.1a-c). Density measurements were made relative to freshwater and

242   expressed in TI where water = 0 HU and air = -1000 HU. We observed Hu unit from -1024 to

243   +616, +499 and +766 on January 14, 16 and 25 respectively. Positive values are related to

244   brine and to a minor extend precipitated salt (e.g. 60 HU < TI < 766 HU) and slightly negative

245   values are related to ice (e.g. TI = -84 HU, Kawamura et al., (1988)). We estimate the

246   tomographic intensity of pure ice crystals using the mode of the histogram (Fig. 1d, TI = -74

247   HU). .

2.7.2 Processing X-ray Images and analysis

249   The process of pixel selection to create binary images of air inclusions, therefore

250   defining the air volume fraction (air porosity, V_a) in the CT imagery was performed by means

251   of thresholding following the determination of a region-of-interest (ROI) created by the

252   removal of all pixels not belonging to the core sample (i.e. the sample container, disturbance

253   of the core edges by coring and/or storage, the supporting bench, and surrounding air from

254   each slice). The images were individually examined and ambiguous pixels around the sea ice

255   core sample were also removed. The bottom slices of each imaged ice core were removed due

256   to observed brine drainage resulting from the coring method. A three-dimensional orthoslice

257   view as well as two transversal slices of the ice core sample extracted on January 16 are

258   shown in Fig. 1. The bottom of the ice core from which brine drainage occurred during core

259   extraction can be clearly differentiated from the rest of the core sample unaffected by brine

260   loss on both the orthoslice and transversal slice views (Fig. 1a-c). CTan and ImageJ software

261 were used to quantitatively measure morphometric characteristics of binary (black and white)

262 images.

263   Determination of the most applicable threshold is therefore of the utmost importance

264 here, as in all image classifications in the multitude of fields that employ the technique. Three

265 approaches are typical for determining an optimal threshold; manual threshold selection based

266 on the human visual system, automated threshold selection based on image data, usually

267 employing the image histogram, and a threshold based on a mixture model approach.

268   There are many automated segmentation techniques described in the literature

269 exceeds. In this study segmentation algorithms representing a selection of established

270 thresholding techniques chosen on the basis that they (i) suited a unimodal histogram (Fig.

271 1d), and they (ii) showed potential for automated characterization of pore space in

272 geomaterials. Global thresholding specifically was selected on the basis of comparative

273 reviews by Sezgin and Sankur, (2004) and Iassonov et al. (2009). Global thresholding may be

274 divided into several subcategories depending on the applied approach. These subcategories in

275 include those based on signal entropy considerations (Shannon and Weaver, 1948; Pal and

276 Pal, 1989; Pal, 1996) to separate background and foreground voxels, including EN-Kapur and

277 EN-Yen (Kapur et al., 1985; Yen et al., 1995). There exist global thresholding methods that

278 analyze histogram shape (HS), including HS-Zack and HS-Tsai (Zack et al., 1977; Tsai,

279 1995). Finally, segmentation may be accomplished by clustering (CL) methods, which

280 separate background (i.e. ice) and foreground voxels (i.e. air) by approximating the histogram

281 with a combination of two or more statistical distributions, including CL-Otsu and CL-Ridler

282 (Ridler and Calvard, 1978; Otsu, 1979).

283   Each segmentation method was tested on the three core image sets (633 total image

284 slices), as well as on selected parts of each image set to insure that the algorithm response was

285 stable. The results of each segmentation method were visually evaluated by comparing the

286 raw and segmented images (Fig. 2) and by computing linear profiles of Hu-value (Fig. 3)

287 through cross-sectional images and examining them visually to determine the efficacy of

288 various thresholds in identifying air inclusions.

289   Analysis of variance (ANOVA) demonstrated significant ($p < 0.005$) differences

290 between in the thresholds produced by the interrogated segmentation methods. The EN-Yen

291 (max-entropy) algorithm produced a relatively high threshold (TI = -200 HU) but also

292 introduced noise and speckle in the image; 66% of 1180 total inclusions detected by the EN-

293 Yen threshold were the size of a single pixel (Fig. 2b, EN-Yen). The HS-Zack (Zack et al.,

294 1977; Rosin, 2001) method produced a low threshold (TI= -569 HU) that (i) did not detect

small bubbles, and (ii) underestimated the size of bubbles detected (Fig. 2c. HS-Zack.). The segmentation threshold produced by the CL-Ridler (TI = -370 HU), method accurately identified bubbles in all images, including detecting very small bubbles, without introducing speckle in the segmented image (Fig. 2d. CL-Ridler).

Manual segmentation thresholds were defined by inspecting a variety of different bubbles in different slices, (e.g. Fig. 3). Figure 3 indicates that visual thresholds were subjective; the pixel scale actually makes visual bubble delineation more ambiguous. Bubble number 2 (Fig. 3) is best delineated by TI = -453 HU, while bubble number 3 (Fig. 3) is best visually delineated by TI = -373 HU. In the context of the variety of bubble morphology and the differences in columnar and granular sea ice in the 633 transverse image slices, the visual segmentation threshold was set at TI = -453 HU.

Finally, the tomographic intensity of "mixed pixels" which appear as varying shades of grey is dependent of the proportion of air (V_{air}), ice (V_{ice}) an brine (V_{brine}) in the pixel and the proportions of the tomographic intensities of those constituents (air ($Hu_{air)}$, ice (Hu_{ice}) and brine (Hu_{brine})) in the following mixture model:

$$Hu = (V_{air} \times Hu_{air}) + (V_{ice} \times Hu_{ice}) + (V_{brine} \times Hu_{brine}) \quad (3)$$
$$1 = V_{air} + V_{ice} + V_{brine} \quad\quad\quad\quad\quad\quad (4)$$

The TI of pure ice crystals is determined using the mode of the histogram containing all the data from each core ($TI_{pure\ ice}$ = -74 HU). Brine TI values ranged from 60 to 500 depending on brine salinity; we selected the middle point of that range (TI_{brine} = 200 HU). Finally TI_{air} = -1000 HU. According to the mixture model (equation (3)), any pixel TI $\geq$ -400 HU contains at least 50% air and is therefore selected as part of an air inclusion (Fig. 2e, Table 2).

The CL-Ridler (TI = -370 HU) threshold, as well as the manual threshold (TI = -453 HU) and the mixture model threshold, which selects pixel containing 50% air (TI = -400 HU) were used to compute the air volume fraction for each of the transverse slices in each of the three ice cores imaged. Analysis of variance (ANOVA) demonstrated no significant difference ($p < 0.005$) between the air volume fraction computed using the mixture model threshold and the air volume fraction computed using the visually defined threshold (TI = -453 HU) or the most applicable automated threshold (CL-Ridler, TI = -370 HU). The CL-Ridler and the visual threshold produced mean V_a values that were statistically different ($p < 0.005$)

329   Hereafter, the air volume fraction is presented as the mean of the air volume fraction

330   results computed using the three selected thresholds. The potential range of the V_a from each

331   of the three methods is represented by the standard deviation of this mean. We are able to

332   compute the V_a in granular layer within a potential range of ±16% and in columnar sea ice

333   within a potential range ±43%.

334   Our method endeavours to meet the challenge of CT X-ray image threshold selection

335   in porous materials while lacking knowledge of the optimal segmentation result. Selecting the

336   most applicable threshold is imperfect because the resolution of the CT-imaged used will

337   almost always be insufficient to resolve every object of interest (in this case air inclusions in

338   sea ice). When the object of interest is smaller than the spatial resolution of the imager, it

339   appears as a mixed pixel, where the tomographic intensity is a combination of air and the

340   presence of ice and/or brine, resulting in voxel TI's than that of pure ice by some amount. In

341   this way delineation of an object using TI thresholds is complicated by the TI's of adjacent

342   pixels/materials. If an air bubble (TI = -1000 HU) is adjacent to both ice (TI = -74 HU,

343   Fig.1d) and brine (TI = 200 HU) the pixel(s) those respective boundaries will be roughly -537

344   on the ice-side and -400 on the brine-side. In granular sea ice where bubble are sufficiently

345   large to be resolve by Ct-scan, mixed pixel concerns mainly the edges of the large and macro

346   bubbles, while in columnar sea ice where bubble are small compared to the pixel size, most of

347   the bubbles appeared as mixed pixels as they include both air and background (ice/brines).

348   We are able to compute the V_a in granular layer within a potential range of ±16% and in

349   columnar sea ice within a potential range ±43%. The morphology of air inclusions is

350   characterized quantitatively using their diameters (Ø, mm) in the transverse (x-y) plane.

351   While it is ambiguous to report exact diameter from mixed pixel, we classified bubble

352   diameters into three categories at a millimeter scale: micro bubbles (Ø < 1 mm), large bubbles

353   (1mm < Ø < 5mm), and macro bubbles (Ø > 5mm).

354   V_a must be clearly differentiated from the GC-derived bulk ice total gas content (in ml

355   L^{-1} ice) which refers to the amount of O_2, N_2, and Ar, both (i) in dissolved phase in brine and

356   (ii) in the gas phase in bubbles measured in 5-cm depth increments. In this work we use the

357   terms "bubbles" and "air inclusions" interchangeably to denote gas phase inclusions in sea

358   ice.

3　Results

3.1　Environmental conditions

At the Sea ice Environmental Research Facility (SERF), the ambient air temperature varied between -5°C and -32°C through the experiment from January 13-26. The average air temperature for the period was -22°C. Three main snowfall events occurred during the experiment. Snowfall on 14 to 15 January covered the sea ice surface with 1 cm of snow. Snowfall from January 19 to 23 deposited 6-9 cm of snow over the entire pool. On the morning of January 23, the snow was manually cleared off the ice surface to investigate the insulating effect of snow on the ice temperature and ikaite precipitation (see Rysgaard et al., 2014). Finally, from January 24 to January 27, 8 cm of snow covered the entire pool until the end of the experiment on January 30. Surface elevation from Lidar data (not shown), indicate that ice surface did not move appreciably in the vertical for the duration of the experiment even as a result of snow removal. Periodically the sea ice froze to the side of the pool resulting in a hydrostatic pressure head in the seawater below, causing episodic percolation of seawater at the freezing point upwards through the sea ice volume resulting in wet snow ice and slush at the sea ice surface on 16 Jan. A slush layer (up to 3 cm thick) was also observed at the snow base on 20 Jan. This episodic hydrostatic pressure head and resultant upward percolation of seawater through the sea ice caused the granular layer of the sea ice volume to thicken over time, likely by the formation of snow ice layers as the slush layer froze. On January 14, the granular layer was 0.7 cm frazil ice, on January 16, the granular layer thickened to 1.7 cm (consisting of the initial 0.7 cm of frazil and 1 cm of snow ice). On January 25, the granular layer had thickened again to 4 cm consisting of the initial granular sea ice layer of 14 Jan, the snow ice layer of 16 Jan and an additional 2.3 cm thick snow ice layer (Fig. 4). Below the granular ice layer, the sea ice crystal texture transitioned nearly immediately to columnar ice on all three dates (Fig. 4).

3.2　Temperatures, salinity, brine volume fraction and bulk ice density

Sea ice temperature, bulk salinity, brine volume and bulk ice density profiles for cores sampled on January 14 (4 cm thick), January 16, (8 cm thick) and January 25 (22 cm thick) are shown in Fig. 5 and Table 3.

On January 14, the bulk salinity profile was approximately linear, and evolved to a more a C-shaped profile on January 16 and 25 as the granular top layer remained saline and the top of the columnar layer desalinated through the experiment (Fig. 5). Calculated brine volume (V_b) profiles were similar in shape to the salinity profiles with minimum V_b occurring

392   in the middle of the columnar ice layer on 16 and 25 Jan (Fig. 5). According to Golden et al.,

393   (1998, 2007) the permeability threshold for columnar sea ice of 5% V_b indicates the whole ice

394   volume on 14 Jan and near the bottom parts of the columnar ice layer on 16 and 25 Jan were

395   permeable to liquid.

396   Bulk ice densities ranged from 0.84 g cm^{-3} ± 0.020 g cm^{-3} to 0.92 g cm^{-3} ± 0.023 g cm^{-}

397   ^{3}. The lowest densities were systematically found at the surface of the ice cover (Fig. 5).

398   3.3   Bulk ice total gas content

399   The total gas content in the sea ice volume increased from its minimum in the bottom

400   permeable columnar layer to its maximum in the top granular layer on 14, 16 and 25 Jan. The

401   total gas content in the sea ice volume also increased over time (Fig. 6). The total gas content

402   of the permeable columnar bottom of each of the ice cores (and the entire core on 14 January)

403   were close to the concentration at saturation with respect to calculated theoretical atmospheric

404   gas concentrations, leading to saturation factor ranging from 0.8 to 1.2. This will be referred

405   to as "subsaturated" (SATf≤1.2). On the contrary, the total gas content of the impermeable

406   columnar layers and the granular surface layers of the sea ice were largely greater than the

407   concentration at saturation leading to saturation factor ranging form 9.5 to 16. These will be

408   referred to as supersaturated (SAT$_f$ > 1.2).

409   3.4   Air Porosity

410   3.4.1   Air volume fraction (V_a) derived from CT X-ray Image Analysis

411   For each of the three dates sampled, the air volume fraction increased from bottom

412   columnar ice layer to the granular surface ice layer and the CT-derived air volume fraction in

413   the sea ice increased overall from 14 to 25 Jan (Fig. 4 and Fig. 7a-c) in the same way as was

414   shown by the total gas content analysis (Fig. 6).

415   In columnar ice, we distinguish permeable (V_b > 5%) and subsaturated (SAT$_f$ ≤ 1.2)

416   ice near the bottom (Fig. 7a and b, shaded blue) from the impermeable (V_b < 5%) and

417   supersaturated (SAT$_f$ > 1.2) ice in the middle sea ice layers (Fig. 7a and b, white area). In the

418   permeable subsaturated bottom sea ice, V_a < 1%, for each sampling date (Table 3). In the

419   intermediate supersaturated impermeable columnar layer, the air volume fraction was

420   typically under 2% and increased from 14 to 25 Jan. At the transition between the

421   impermeable columnar ice and the permeable columnar ice on 16 and 25 Jan (Fig. 7c, shaded

422   pink), we observed a slight increase in V_a.

423   On all three dates, the maximum air volume fraction occurred in the granular layers

424 nearest the atmosphere interface increasing from the base of the granular layer (Fig. 7c and d).

425 As the granular ice layer thickened by snow ice formation from 0.7 cm to 4 cm, V_a in these

426 layers increased (Fig. 7c and d). In the granular layers, the brine volume exceeded 5% (Fig. 5)

427 and the saturation factor > 9 on 16 and 25 Jan (Fig. 6).

428 **3.4.2 Air inclusion morphology**

429   The morphology of air inclusions is characterized quantitatively using their diameters

430 (Ø, mm) in the transverse (x-y) plane (Fig. 8). We classified CT-derived bubble diameters

431 into three categories: micro bubbles (Ø < 1 mm), large bubbles (1mm < Ø < 5mm), and macro

432 bubbles (Ø > 5mm) (see for e.g. Fig. 8). Bubbles smaller than the pixel size (0.0097 mm in the

433 transverse plane) represented less than 10% of the bubble population in any type of ice except

434 for the impermeable supersaturated columnar layer on 16 Jan (Fig. 9a). Most of the bubbles

435 had diameters ≤1 mm; bubbles of this size were common at every depth in every ice type

436 interrogated by the CT imager (Fig. 9a and b). Due to the non-destructive nature of the CT X-

437 ray method we were able to observe larger bubbles with diameters as large as 18.3 mm in

438 granular sea ice (Fig. 9b).

439   For each ice core, the bubble size increased from the bottom columnar layer, to the top

440 granular layer and increased over time in the same way as observed by the total gas content

441 measured using the GC method (Fig. 9b). The bottom permeable subsaturated columnar ice

442 contained almost exclusively micro bubbles on all three dates (Fig. 9a and b). Large bubbles

443 occurred more frequently in the intermediate impermeable supersaturated columnar layer than

444 in the bottom permeable and subsaturated columnar layer. Macro bubbles (Ø > 5 mm) were

445 exclusively found close to the ice-atmosphere interface in the snow ice layer (Fig. 9b).

446 **4   Discussion**

447 **4.1 Computed tomography X-ray imaging as a non destructive method to**
448 **compute the sea ice air volume fraction**

449   By using computed tomography X-ray imaging with a voxel size of 0.0056 mm^3 we

450 provide high-resolution profiles of the vertical distribution of air inclusions in sea ice, from

451 which the sea ice air volume fraction are computed every 0.6 mm. Taking into account the

452 potential range of $V_a \pm 16\%$ in granular layer and $V_a \pm 43\%$ in columnar ice, results of image

453 analysis indicated that the air volume was < 1% in most of the columnar ice, but

454 systematically reached 5% in the granular/snow ice top layer where an air volume fraction as
455 high as 19% was observed.

456   CT X-ray images (of porous materials in particular) are of such high resolution (in this
457 case voxel = 0.0056 mm^3), use such large sample volumes and are so quick that traditional
458 methodology can hardly be used to validate the imaged data at the same resolution.
459 Nevertheless, we compared our CT-derived V_a results, to air volume fraction computed based
460 on density measurements (Cox and Weeks, 1983) (Fig. 10a). The density (M/V) derived air
461 volume profiles were generally slightly larger (Fig. 10a) but the two methods generally agree
462 ($R^2 = 0.97$) (Fig. 10b). The precision in density-derived V_a is very low (±163%), compared
463 with the relative standard deviation from CT- derived volume fraction of $V_a ± 16\%$ in
464 granular layer and $V_a ± 43\%$ in columnar sea ice. The CT-derived air volume fraction also
465 compared to the bulk ice total gas content (ml L^{-1} ice) data derived from the GC analysis
466 (using 60 g samples from 5-cm thick sections) (Fig. 10c). The vertical gradients in the two
467 datasets increased similarly from the ice bottom to the sea ice surface and both the total gas
468 content (ml L^{-1} ice) and the CT-derived air volume fraction increased as the ice thickened
469 over time.

470   Correlation between CT-derived air volume fraction and the bulk ice gas content (ml
471 L^{-1} ice; Fig. 10c) is not straightforward due in part to methodological constraints. The data
472 agreed well in columnar sea ice while in granular layer, we observed large deviations. In
473 granular ice, the total gas content was much lower than the CT-derived air volume fraction.
474 CT image voxels are 0.0056 mm^3, whereas the bulk ice total gas content was measured on 5-
475 cm sections. Those 5-cm thick sections did not always resolve the changes in ice type. Within
476 the 5-cm sections, gas might span a large range of concentration as does the air volume
477 fraction in granular sea ice (Fig.10b, error bar); therefore if thinner sections had been
478 analyzed for the total gas content (ml L^{-1} ice) the values obtained might have been higher in
479 the top part of the ice core, similar to the CT image data. Moreover, the measurement of the
480 total gas content is a destructive sampling process, involving multiple steps in which the gas
481 could potentially leave the ice. During the cutting process, some bubbles are inevitably cut in
482 half, so part of the gas is lost. This is further complicated by the fact that the probability of
483 cutting a large bubble (with high gas content) is greater than for a small bubble with low gas
484 content. Potential gas loss could also happen during the evacuation phase of the measurement
485 of the total gas content (i.e.. section 2.3). For all these reasons, the total gas content (ml L^{-1}
486 ice) is likely to be particularly underestimated in the granular surface ice due the analytical
487 procedure. The data however agree well in columnar sea ice. The bulk ice total gas content

488   measured by gas chromatography includes both gas dissolved in brine and gas trapped in

489   bubbles, while CT-derived air volume fraction results only account for gas trapped in bubbles.

490   Then, we expect the total gas content values to be slightly higher than the CT-derived air

491   volume fraction due to the dissolved contribution. In reality, the total gas content appears to

492   be slightly lower (Figure 10c). It suggests that either the CT-derived air volume fraction is

493   slightly overestimated in columnar sea-ice due to the thresholding process or that the total

494   bulk gas is slightly underestimated due to gas loss during the cutting and evacuation phase of

495   the measurement process. Finally, the bulk ice total gas content was measured on different ice

496   cores from those used for the CT measurements, which may have introduced some spatial

497   variability.

498   The storing temperature finally potentially influences our computation. Storing

499   sea ice at -20°C alters the sea ice microstructure and its inclusions (e.g. Cox and Weeks,

500   1986). Light et al., (2003) proceeded to a cooling sequence (-2°C to -25°C) and a warming

501   sequence (-25°C to -2°C) on ice thin sections. According to their results cooling sea ice

502   caused inclusions to shrink in size including the disappearance of the smallest air inclusions,

503   while warming increased the size of existing air inclusions without forming new bubbles.

504   Considering that the smallest bubbles could have disappeared and some have shrunk in size,

505   our computed air volume fraction should be considered as a minimum estimate of the true air

506   volume fraction. In the absence of a method that preserves the natural temperature gradient

507   within sea ice immediately and without change upon extraction, ex situ analysis of sea ice

508   samples after storage at low temperatures is an established protocol.

509   Although microstructural analysis of sea ice may produce reliable morphological results

510   for air inclusions, thin sections only represent a small subsample of the ice core, are time

511   consuming, can be operator-dependent, and the area and thickness of a thin section limit these

512   studies to the measurement of intact bubbles within a thin section. Density-derived air volume

513   fraction results from the Mass-Volume technique generally have large errors and very low

514   vertical resolution because they require large core subsample volumes (e.g. 5 cm^3). On the

515   contrary, CT X-ray imaging clearly distinguishes between air inclusions and the ice matrix

516   providing high-resolution sub-millimeter profiles of the air volume vertical distribution with a

517   better precision linked almost entirely to the segmentation process and the resolution of the

518   scanner. X-ray tomography allows: (1) fast visualisation of the air inclusions, especially when

519   compared to transmitted images; (2) the ability to increase the size of the dataset compared to

520   thin section microstructural analysis by imaging the whole core. Future work should involve

521   micro CT –X-ray with a voxel resolution of 15 μ m to detect the small bubbles in columnar

522   sea ice as well as the effect on temperature changes on sea ice gas inclusions.

523   **4.2   Size of the air inclusion (i.e. bubbles): Micro, large and macro air porosity**

524   While large and macro bubbles account for less than 17%, 24% and 27% of the bubble

525   population observed for January 14, 16 and 25 respectively (Fig. 11a), the large and macro

526   bubbles contribute systematically to more than 50% of the total air volume fraction produced

527   (Fig. 11a). Even in bottom columnar ice where large bubbles represent only 10% of the

528   bubble population (Fig. 11d), they contributed to 40 % and 22 % of the air porosity of bottom

529   columnar ice on January 14 and 25 respectively (Fig. 11d). For each ice types (Fig. 11,

530   granular (b.), columnar impermeable (c.) and columnar permeable (d.)), it is clear that sea ice

531   air volume fraction is largely controlled by the size of the air inclusions rather than their

532   number (Fig. 11, Table 4). The presence of large and macro bubble causes the air volume

533   fraction to increase exponentially in each ice layer. However in columnar sea ice where the

534   proportion of large bubbles decreased and where most of the air volume fraction is < 2% (Fig.

535   12) increasing the number of bubbles produces also a linear increase in the air volume fraction

536   (Fig. 12). For the air volume fraction to increase above 3% (e.g. Fig. 12 in the granular

537   layer), the presence of large and macro bubbles are required (Fig. 12).

538   Large bubbles were more prevalent when brine volume increased (Fig.13a, red and grey

539   circles). Light et al. (2003) observed that bubbles were contained within brine and concluded

540   that bubble size was limited by the size of the brine inclusion in which they resided. In several

541   slices, we observed lighter pixels around air inclusions indicating these bubbles likely formed

542   in a brine pocket. The CT-scanner used here cannot unambiguously identify these pixels as

543   brine inclusions. To visualize both air and brine inclusions in the same images, finer

544   resolution with respect to sample density and finer spatial resolution are required. For

545   example, Obbard et al. (2009) showed that micro-X-ray computed tomography with a voxel

546   resolution of 15 μ m is suitable for visualisation of brine and air inclusions.

547   **4.3   Mechanism for gas incorporation and bubbles development**

548   In our sea ice samples, the top granular layers are supersaturated, have large air

549   volume fractions (V_a > 5%) and contain macro bubbles. The impermeable columnar layers are

550   supersaturated as well but contain lower air volume fractions (V_a < 2%) and contain micro to

551   large bubbles. The bottom permeable columnar layers are subsaturated, contain air volume

552   fractions <1%, and contain almost exclusively micro bubbles (see summary Table 5).

553   In the multiphase sea ice system, the ratio between dissolved gas and bubbles should

554   depend on the bulk ice gas saturation state. In a closed system, when bubble nucleation is

exclusively solubility driven, we expect the air volume fraction to be a function of the saturation factor, which would lead to subsaturated sea ice being bubble-free, and high air volume fractions in supersaturated sea ice. However, the observed relationship between air volume fraction and saturation factor is not straightforward (Fig. 13b) and highlights difference between the type of ice (i) bottom permeable columnar ice, (ii) intermediate impermeable columnar ice and (iii) top granular ice.

4.3.1 Bottom permeable columnar ice

Within the permeable subsaturated columnar layer near the sea ice bottom, the air volume fraction is lower than 1 % due to the subsaturated state of the ice, and independent of the brine volume fraction (Fig. 13a and b, blue circles). As long as the brine is able to exchange with the underlying seawater (i.e. when the V_b is > 5% after Golden et al., 1998), the saturation factor remains low and gas species remain dissolved in the brine and can be rejected to the underlying water by convection from the permeable columnar layer. This limits bubble formation, and hence the air volume fraction was < 1% (Fig.13a and b, blue circles). Although the air volume fraction is low in these layers, it is somewhat surprising that the air volume fraction is > 0; in theory, bubble nucleation occurs when SAT_f > 1, so these subsaturated layers should be bubble-free, though bubble nucleation from saturated gas solutions has been observed at much lower saturations than theoretically expected (Lubetkin, 2003). On January 14, 75% of the bubbles observed were located in subsaturated permeable bottom layer of columnar sea ice. On January 16 and 25, 11% and 13% (respectively) of the air inclusions observed were situated in subsaturated permeable sea ice. Bubble nucleation processes are favoured where (i) there are geometrical imperfections (Wilt 1986); (ii) at "active sites" on a heterogeneous surface that can be chemically, structurally, or geometrically inhomogeneous (Deutscher and Fletcher, 1990; Kozisek et al. 2000); and (iii) by heterogeneous supersaturation away from thermodynamic equilibrium (Li and Yortsos 1994), conditions which are all met in sea ice. The contact of the tree-phase (solid ice, liquid brine, air bubble and precipitated salt) in brine inclusions produced a highly heterogeneous surface, which is both chemically and structurally inhomogeneous. Moreover, full-depth convection on January 14 and convection confined to the permeable subsaturated bottom columnar layer of sea ice ($V_b \approx 20\%$) on 16 and 25 January likely produced local fluctuations in the amount of gas-saturated liquid, creating the possibility of local or episodic supersaturation that may have produced bubbles as has been observed by Zhou et al., (2013). Convection driven nucleation processes likely produced micro bubbles in columnar permeable sea ice, which

588   contributed to 8.4% of the total air volume fraction observed (Table 6.). Therefore, brine

589   drainage is only effective for the transport of dissolved gases to the underlying seawater. The

590   rejection of dissolved gas contributes to maintain gas concentrations close to the equilibrium.

591   Nucleation processes driven by the convective exchange in the bottom layer however limited

592   by the saturation state increase the total gas content (ml L^{-1} ice) of sea ice by ensuring that gas

593   trapped in bubbles remains within the sea ice and is not rejected to the underlying water

594   (Tison et al., 2002).

595   On January 16 and 25, we observed a slight increase of air volume fraction at the

596   transition between the subsaturated and permeable columnar sea ice and the supersaturated

597   impermeable columnar sea ice at two-thirds of the total sea ice thickness (isotherm -4.1°C and

598   -3.8°C, respectively) (Fig. 7b, shaded pink area). This imparts that bubbles created by

599   convection-driven nucleation in the permeable bottom layer, naturally accumulate at the brine

600   permeability transition as result of their buoyancy, trapped when the sea ice matrix becomes

601   impermeable to liquid. Our work indicates that brine will start to supersaturate (SAT_f = 2.7 to

602   5) under cooling (isotherm -4.1°C and -3.8°C, respectively) when the sea ice begins to

603   become vertically impermeable to liquid, leading to solubility-driven nucleation. We could

604   expect that at any given time, a local air volume fraction maxima is located above the

605   permeability transition.

4.3.2 Intermediate impermeable columnar sea ice

607   Within the supersaturated impermeable columnar layer, bubble nucleation is solubility

608   driven and we expect the air volume fraction to be a function of the saturation factor. Within

609   the supersaturated impermeable columnar layer, the air volume fraction becomes increasingly

610   a function of the saturation factor as the brine volume increases (Fig. 13b, red circles). At low

611   brine volumes, the air volume fraction is low regardless of the saturation factor, as indicated

612   by the accumulation of red circles in the top left corner of Fig. 13b. As brine volume increases

613   in the impermeable supersaturated intermediate columnar layer, both air volume fraction and

614   bubble size increase (Fig. 13a and b). At a given SAT_f, there are more gas molecules available

615   to go into the gas phase when brine volume increases, thereby increasing the air volume

616   fraction and the size of existing bubbles. We therefore suggest that bubble nucleation is a

617   function of the saturation factor as well as the brine volume. Solubility-driven nucleation

618   produced micro bubbles and large bubbles depending on the brine volume in this layer,

619   contributed 44% of the total observed air volume fraction (Table 6).

4.3.3 Granular sea ice

We observed an increase of air volume fraction nearest the ice-atmosphere interface and generally within the ice surface granular ice layer (Figs 7d-e. and 9b). This granular surface layer had the highest gas content, the highest saturation factor, the highest air volume fraction ($5\% < V_a < 19.4\%$) and contained bubbles with diameters as large as 4.5, 13, and 18 mm on January 14, 16 and 25, respectively (Table 5). The increase of air volume fraction and the total gas content (largely underestimated) in the surface granular layer can be explained by a combination of several processes.

The formation of frazil ice is well known to contain more gas than columnar ice because it traps gas directly from the atmosphere (Tsurikov, 1979; Cole et al., 2004, Zhou et al., 2013) can explain the air volume fraction in the sea ice formed on January 14. Snow-ice formation observed thereafter on 16 and 25 January trapped gas initially contained within the snow. Moreover, rapid freezing of slush forces gas out of solution, building up the air volume fraction nearest the ice-atmosphere interface.

Macro bubbles are exclusively found in granular layer. They seems resulting of aggregation of discrete bubble like an aggregation of soap bubbles A succession of 0.6 mm thick transversal slices at 2.46 cm depth from January 25 is shown in Fig.14. In the first slice at +2.28 cm depth (Fig. 14, far left panel) four individual bubble bases are identifiable from which a single top bubble is formed at +2.46 cm depth (Fig.14 far right panel). The rapid freezing of slush in porous snow could potentially produce bubble aggregation. Granular sea ice and snow ice accounted for 26% of the bubble population observed, and snow ice formation accounted for 47% of the total porosity recorded indicating that physical processes associated with snow on new and young sea ice play an important role in the gas dynamics of new and young sea ice.

4.4 The fate of gas versus the fate of salt

Bulk salinity and bulk ice total gas content (ml L^{-1} ice) of sea ice is lower than in the seawater from which it formed, because gases in seawater are preferentially expelled from growing ice, along with salts (Cox and Weeks, 1983, 1988; Killawee et al., 1998; Tison et al., 2002, Loose et al., 2009, 2011). The range of total gas content values for our samples was 1.6 to 6.5 mL L^{-1}, which is in the lower end of ranges reported by Matsuo and Miyake (1966), Tison et al., (2002) and Crabeck et al., (2014b). Zhou et al., (2013) suggested that gas transport through sea ice occurs via processes diverging from those controlling the transport of salt. Since we do not observe similar profiles of these two parameters over time, this also

653   suggests that the same processes do not regulate bulk ice salinity and bulk ice gas content.
654   Rapid desalinisation occurred between January 14 and January 16, and the bulk salinity
655   profile evolved towards a C-shaped profile over time (Fig. 5). In contrast, we observed a
656   linear increase of gas content (ml L^{-1}) (Fig. 6) and air volume fraction (Fig. 7) from the base
657   to the sea ice surface and within sea ice as it thickened over time. The transport of gases
658   through sea ice is different from that of the solutes because gases may be present in the form
659   of bubbles, on top of being dissolved in the brine. Our results indicate that a great deal of the
660   air volume fraction of sea ice exists in bubbles and not in the dissolved phase in brine,
661   suggesting that desalination processes have a limited effect on sea ice gas content. Salts
662   dissolved in brine can diffuse and/or be rejected in the underlying seawater during brine
663   convection events, while bubbles are trapped in the ice matrix and can only migrate upward
664   by buoyancy.

665   The presence of large bubbles and air volume fraction > 5% in the top of the ice cover
666   should potentially mediate gas fluxes over sea ice. Partitioning between gaseous phase and
667   dissolved phase is of paramount importance for gas transport in sea ice, as it control the
668   direction of transport – upward versus downward as well as the magnitude. If the gases are in
669   the dissolved phase, they will be mainly transported downwards with the brines, like the other
670   solutes. Few exceptions are the gas diffusion within the brines network that transport gases
671   both ways in function of the concentration gradient (Crabeck et al., 2014a), and upward brine
672   expulsion at the ice-air atmosphere. If the gases are in the gas phase (i.e. bubbles), they are
673   only transported upward due to bubbles buoyancy. Kotovich et al., (2015) observed that air-
674   ice gas transfer coefficients for CO_2 in young permeable artificial sea ice is 5 times larger
675   during ice growth compared to ice decay. They suggest that this difference is due to the
676   formation and transport of bubbles during ice growth. This process appears to provide a very
677   efficient pathway to transport gases within and out of the ice. Indeed, 1D modelling suggests
678   that bubbles migrating upward out of the ice contribute to 80% of the CO_2 fluxes from sea ice
679   to the atmosphere during ice growth (Kotovich et al., (2015).

680   **5   Conclusions and perspectives**

681   We used computed tomography X-ray imaging to quantify air inclusion distribution in
682   sea ice, from which we derive the air volume fraction. Air inclusions are quickly and easily
683   identified by X-ray tomography and quantitatively analyzed using segmentation techniques.
684   The threshold selection is a crucial step requiring careful examination to provide successful
685   results. The results from the CT X-ray analysis showed similar trends to conventional density

686 and bulk ice total gas content (ml L^{-1} ice) measurement methods. X-ray imaging is non-
687 destructive and allows for a direct determination of air inclusions in sea ice at high resolution
688 with low errors and creates large datasets very quickly. However, the medical CT-scan show
689 some limitation to resolve air inclusions in columnar sea ice, since accurate definition of air
690 inclusion in columnar sea ice would require higher resolution. Further studies should involve
691 Micro-Ct scan with pixel size of 15 μm

692 We differentiate between micro bubbles, large bubbles and macro bubbles based on
693 their diameters. Micro bubbles are found both in the bottom columnar permeable layers ($V_b >$
694 5%) and in the intermediate columnar impermeable layers ($V_b < 5\%$) as well as in granular
695 layers. Large bubbles are found more frequently where brine volume exceeded 5% and macro
696 bubbles occur exclusively in the granular snow ice layer nearest the ice-atmosphere interface.
697 Although micro bubbles are the most abundant type of bubbles observed, they only accounted
698 for 14 % of the total air volume fraction recorded. In contrast, macro bubbles linked to
699 granular snow ice layer accounted for 1 % of the total number of bubbles but their size
700 (volume) accounts for 24% of the total air volume fraction of the sea ice imaged. While the
701 air volume fraction results from a mix of micro, large and macro bubbles, the factor
702 controlling the air volume fraction is most likely the size of the air inclusions (i.e. bubbles)
703 (Table 4).

704 We suggest that bubbles observed in the bottom subsaturated permeable layers are
705 formed by convection-driven nucleation. Here the amount and size of the bubbles are limited
706 by the low saturation state of the brine. Bubbles observed in impermeable columnar
707 supersaturated sea ice are formed by solubility-driven nucleation, where the amount and
708 bubble size is limited by the amount of brine. In growing sea ice, a local maximum exists at a
709 given depth just above the permeability transition, confirming the important role of this
710 transition zone in shaping the vertical air volume fraction distribution. Macro bubbles located
711 in the near-surface sea ice are linked to the presence of granular ice and the formation of snow
712 ice (Table 6).

713 We conclude that processes regulating the vertical distribution of salts do not control
714 the vertical distribution of gases, because most of the total gas content (ml L^{-1} ice) exists as
715 bubbles rather than being dissolved in the brine as previously argued (Tison et al., 2002; Zhou
716 et al., 2013, Moreau et al., 2014, Crabeck et 2014a, b). Once micro and/or macro bubbles
717 form they are segregated from the transport pathway of dissolved salts, because bubbles will
718 not drain out of the ice by convection due to their low density, so nucleation leads to an

719 accumulation of gas in sea ice. Our work provides the first detailed visual demonstration and
720 quantification of these processes.

721 As a result of the presence of large bubbles and higher air volume fraction
722 measurements in sea ice we introduce new perspectives on processes regulating gas exchange
723 at the ice-atmosphere interface, and note that further work should investigate, the effect of air
724 volume fraction on sea ice permeability parameterizations. CT-X-ray imaging may allow for
725 visualizations of transport pathways, for example the upward migration of bubbles. CT-X-ray
726 imaging could be used to investigate the effect of different thermal and crystal texture regimes
727 on bubble formation, dimensions, and their vertical and horizontal distribution in a large
728 number of replicate cores from the same ice cover. This information is vital to the
729 improvement of models involving transport of biochemical compounds and gas transfer
730 between the ocean and the atmosphere in polar oceans.

731

References

Bennington, K. O.: Desalination features in natural sea ice, Journal of Glaciology, 6(48): 845-857,1967.

Bock, C., and Eicken, H.: A magnetic resonance study of temperature-dependent microstructural evolution and self-diffusion of water in Arctic first-year sea ice, Annals of Glaciology, 40: 179 – 184, 2005.

Boespflug, X., Ross, N., Long, B. and Dumais, J.F.: Axial tomodensitometry: correlation between tomographic intensity and density of materials, Can. J. Earth Sci., 31, 426–434, 1994.

Carte, A. E.:Air bubbles in ice, Proceedings of the Physical Society, 77(495), 757-768, 1961.

Cole, D. M. and Shapiro, L. H.: Observations of brine drainage networks and microstructure of first-year sea ice, Journal of Geophysical Research, 103(C10): 21739-21750,1998.

Cox, G. F. N. and Weeks, W. F.: Brine drainage and initial salt entrapment in sodium chloride ice, Cold Regions Research and Engineering Laboratory Research Report 345. Hanover, NH, 1975.

Cox, G. F. N., and Weeks W. F.: Equations for determining the gas and brine volumes in sea-ice samples, Journal of Glaciology, 29(102), 306 – 316, 1983.

Cox, G.F.N., Weeks, W.F.: Changes in the salinity and porosity of sea-ice samples during shipping and storage. J. Glaciol. 32 (112), 371–375, 1986.

Crabeck, O., Delille, B., Else,.B, Thomas, D. N., Geilfus, N. X., Rysgaard, S., and Tison, J. L.: First ''in situ'' determination of gas transport coefficients (DO2 , DAr, and DN2) from bulk gas concentration measurements (O2, N2, Ar) in natural sea ice, J. Geophys. Res.-Oceans, 119, 6655–6668, doi:10.1002/2014JC009849, 2014a.

774 Crabeck, O., Delille, B., Thomas, D. N., Geilfus, N. X., Rysgaard, S., and Tison, J. L.: CO2
775 and CH4 in sea ice from a subarctic fjord, Biogeosciences Discuss., 11, 4047-4083,
776 doi:10.5194/bgd-11-4047-2014, 2014b.
777
778 Delille B., Vancoppenolle M., Geilfus N.-X., Tilbrook B., Lannuzel D., Schoemann V.,
779 Becquevort S., Carnat G., Delille D., Lancelot C., Chou L., Dieckmann G.S. and Tison J.-L. :
780 Southern Ocean CO2 sink: The contribution of the sea ice, Journal of Geophysical Research:
781 Oceans, 119, 6340–6355 doi:10.1002/2014JC009941, 2014.
782
783 Duliu, O.G.: Computer axial tomography in geosciences: An overview. Earth-Science
784 Reviews,48, 265-281,1999.
785
786 Garcia, H. E., and Gordon, L. I.: Oxygen solubility in seawater - better fitting equations,
787 Limnology and Oceanography, 37(6), 1307-1312,1992.
788
789 Eicken, H., Bock, C., Wittig, R., Miller, H., and Poertner, H.-O.: Magnetic resonance imaging
790 of sea-ice pore fluids: methods and thermal evolution of pore microstructure, Cold Regions
791 Science and Technology, 31, 207-225, 2000.
792
793 Eide, L. I. and Martin, S.: The formation of brine drainage features in young sea ice, Journal
794 of Glaciology, 14(70: 137-154, 1975.
795
796 Feltham, D. L., Untersteiner, N., Wettlaufer, J. S. and Worster, M. G.: Sea ice is a mushy
797 layer, Geophysical Research Letters, 33, L14501, doi: 10.1029/2006GL026290, 2006.
798
799 Fritsen, C. H., Lytle, V. I., Ackley, S. F., and Sullivan, C. W.: Autumn bloom of Antarctic
800 pack-ice algae, Science, 266(5186): 782-784, 1994.
801
802 Galley, R. J., Else, B. G. T., Geilfus, N.-X., Hare, A. A., Isleifson, D., Barber, D. G. and
803 Rysgaard S.: Imaged brine inclusion in young sea ice – Shape, distribution and formation
804 timing, Cold Regions Science and Technology, 111, 39-48,
805 doi :10.1016/j/coldregions.2014.12.011, 2015a.
806
807 Galley, R. J., Else, B. G. T., Geilfus, N.-X., Hare, A. A., Babb, D., Papakyriakou, T., Barber,

808   D. G. and Rysgaard, S.: Micrometeorological control of frost flower growth and decay on

809   young sea ice, Arctic, 68(1) :79-92, doi : 10.14430/arctic4457, 2015b.

810

811   Garcia, H. E., and Gordon L. I.: Oxygen solubility in seawater: Better fitting equations,

812   Limnology and Oceanography, 37(6), 1307-1312,1992.

813

814   Geilfus, N.-X., Tison, J.-L., Ackley, S. F., Rysgaard, S., Miller L.A. and Delille, B.: Sea ice

815   pCO2 dynamics and air-ice CO2 fluxes during the Sea Ice Mass Balance in the Antarctic

816   (SIMBA) experiment - Bellingshausen Sea, Antarctica, The Cryosphere, 8, 2395-2407,

817   doi:10.5194/tc-8-2395-2014, 2014.

818

819   Geilfus, N.-X, Galley, R.-J, Crabeck, O., Papakyriakou, T., Landy, J., Tison, J.-L.: Inorganic

820   carbon dynamics of melt pond-covered first year sea ice in the Canadian Arctic

821   Biogeosciences Discussions 11, 7485-7519, 2015.

822

823   Golden, K.M., Ackley, S.F., and Lytle, V.I.: The percolation phase transition in sea ice,

824   Science, 282, 2238-2241, 1998.

825

826   Golden, K.M., Eicken, H., Heaton, A.L., Miner, J., Pringle, D.J., and Zhu, J.: Thermal

827   evolution of permeability and microstructure in sea ice, Geophys. Res. Lett., 34,

828   L16501,doi:10.1029/2007GL030447, 2007.

829

830   Grenfell, T. C., A theoretical model of the optical properties of sea ice in the visible and near

831   infrared, J. Geophys. Res., 88, 9723–9735, 1983.

832

833   Hamme, R. C., and Emerson, S. R.: The solubility of neon, nitrogen and argon in distilled

834   water and seawater, Deep-Sea Research Part I-Oceanographic Research Papers, 51(11), 1517-

835   1528, 2004.

836

837   Hare, A. A., Wang, F., Barber, D., Geilfus, N.-X., Galley, R. J., and Rysgaard, S.: pH

838   evolution in sea ice grown at an outdoor experimental facility, Marine Chemistry, 154: 46-54,

839   doi: 10.1016/j.marchem.2013.04.007, 2013.

840

841 Hounsfield, G.N. :Computerized transverse axial scanning (tomography). Part 1: Description
842 of system. British Journal of Radiology, 46, 1016-22, 1973.

843

844 Hunter, M. W., Dykstra, R., Lim, M. H., Haskell, T. G., and Callaghan, P. T.: Using Earth's
845 field NMR to study brine content in Antarctic sea ice: Comparison with salinity and
846 temperature estimates, Applied Magnetic Resonance, 36: 1 − 8, doi: 10.1007/s00723-009-
847 0003-9, 2009.

848

849 Iassonov, P., Gebrenegus, T. and Tuller, M.:Segmentation of X-ray computed tomography
850 images of porous materials: A crucial step for characterization and quantitative analysis of
851 pore structures, Water Resour. Res., 45, W09415, doi:10.1029/2009WR008087, 2009.

852

853 Jones, S. F., Evans, G. M. and Galvin, K. P.: Bubble nucleation from gas cavities - a review,
854 Advances in Colloid and Interface Science, 80, 27-50, 1999.

855

856 Kapur, J. N., Sahoo, P. K. and Wong, A. K. C.: A new method for gray-level picture
857 thresholding using the entropy of the histogram, Graphical Models Image Process., 29, 273 −
858 285, doi:10.1016/0734- 189X(85)90125-2, 1985.

859

860 Kawamura, T. :Observations of the internal structure of sea ice by X ray computed
861 tomography, J. Geophys. Res., 93(C3), 2343–2350, doi:10.1029/JC093iC03p02343, 1988.
862

863 Killawee, J.A., Fairchild, I.J., Tison, J.L., Janssens,L., and Lorrain, R.: Segregation of solutes
864 and gases in experimental freezing of dilute solutions: Implications for natural glacial
865 systems, Geochimica Et Cosmochimica Acta, 62, 3637-3655, 1998.

866

867 Knoll GF.: Radiation Detection and Measurment. John Wiley &Sons: New York,1989.

868

869 Krembs, C., Gradinger, R., and Spindler, M.: Implications of brine channel geometry and
870 surface area for the interaction of sympagic organisms in Arctic sea ice, Journal of
871 Experimental Marine Biology and Ecology, 243: 55-80, 2000.

872

873 Langway, C. C.: Ice fabrics and the universal stage Rep. 62, U.S. Snow, Ice and 496
874 Permafrost Research Establishment, Wilmette, Illinois, 1958.

875

876 Light, B., Maykut, G. A. and Grenfell, T.C.: Effects of temperature on the microstructure of

877 first-year Arctic sea ice, J. Geophys. Res., 108, 3051, doi:10.1029/2001JC000887, C2, 2003.

878

879 Loose, B., McGillis, W.R., Schlosser, P., Perovich, D., and Takahashi, T.: Effects of freezing,

880 growth, and ice cover on gas transport processes in laboratory seawater experiments,

881 Geophysical Research Letters, 36, L05603, L05603 10.1029/2008gl036318, 2009.

882

883 Loose, B., Schlosser, P., Perovich, D., Ringelberg, D., Ho, D.T., Takahashi, T., Richter-

884 Menge, J., Reynolds, C.M., McGillis, W.R., and Tison, J.L.: Gas diffusion through columnar

885 laboratory sea ice: implications for mixed-layer ventilation of CO_2 in the seasonal ice zone,

886 Tellus Series B-Chemical and Physical Meteorology, 63, 23-39, 10.1111/j.1600-

887 0889.2010.00506.x, 2011.

888

889 Lubetkin, S. D.: Why is it much easier to nucleate gas bubbles than theory predicts?

890 Langmuir, 19, 2575– 258, 2003.

891

892 Moreau, S., Vancoppenolle, M., Zhou, J., Tison, J.-L., Delille, B., and Goosse, H.: Modelling

893 argon dynamics in first-year sea ice, Ocean Modelling, 73(0), 1-18, 2014.

894

895 Matsuo, S., and Miyake, Y.: Gas composition in ice samples from Antarctica, Journal of

896 Geophysical Research, 71, 5235-5241, 1966.

897

898 Nomura, D., Yoshikawa-Inoue, H., and Toyota, T.: The effect of sea-ice growth on air-sea

899 CO_2 flux in a tank experiment, Tellus Series B-Chemical and Physical Meteorology, 58, 418-

900 426, 2006.

901

902 Nomura, D., Yoshikawa-Inoue, H., Toyota, T. and Shirasawa. K. : Effects of snow, snow-

903 melting and re-freezing processes on air-sea ice CO_2 flux, J. Glaciol., 56(196), 262–270,

904 2010.

905

906 Notz, D., and Worster. M. G.: In situ measurements of the evolution of young sea ice, J.

907 Geophys. Res., 113, C03001, doi:10.1029/ 2007JC004333, 2008.

908

909 Obbard, R., Troderman, G., Baker, I.: Imaging brine and air inclusions in sea ice using micro-

910 X-ray computed tomography, correspondance, J. Glaciol., 55, 1113–1115, 2009.

911

912 Otsu, N. : A threshold selection method from gray-level histograms, IEEE Trans. Syst. Man

913 Cybern., 9, 62 – 66, doi:10.1109/TSMC.1979.4310076, 1979.

914

915 Pal, N. R. : Minimum cross entropy threshold selection, Pattern Recognition, 29, 575–580,

916 doi:10.1016/0031-3203(95)00111-5, 1996.

917

918 Pal, N. R., and S. K. Pal. : Entropic thresholding, Signal Process., 16, 97–108,

919 doi:10.1016/0165-1684(89)90090-X, 1989.

920

921 Papakyriakou, T., and Miller,L.: Springtime CO_2 exchange over seasonal sea ice in the

922 Canadian Arctic Archipelago, Annals of Glaciology, 52(57), 215-224, 2011.

923

924 Perovich, D. K., and A. J. Gow. : A quantitative description of sea ice inclusions, Journal of

925 Geophysical Research: Oceans, 101(C8), 18327-18343, 1996.

926

927 Pringle, D. J., Miner, J. E., Eicken, H. and Golden, K. M. : Pore space percolation in sea ice

928 single crystals, J. Geophys. Res., 114, C12017, doi:10.1029/2008JC005145, 2009.

929

930 Raynaud, D., Delmas, R., Ascencio, M., and Legrand, M.: Gas extraction from polar ice

931 cores: a critical issue for studying the evolution of atmospheric CO_2 and ice-sheet surface

932 elevation, Annals of Glaciology, 3, 265-268,1982.

933

934 Rees Jones D. W., and Worster, M. G.:A simple dynamical model for gravity drainage of

935 brine   from   growing   sea   ice,   Geophysical   Research   Letters,   40:1-5,   doi:

936 10.1029/2012GL054301,2013.

937

938 Ridler, T. W., and Calvard, S.: Picture thresholding using an iterative selection method, IEEE

939 Trans. Syst. Man Cybern., 8, 630–632, 1978.

940

941 Rysgaard, S., Wang, F., Galley, R. J., Grimm, R., Notz, D., Lemes, M., Geilfus, N.-X.,

942 Chaulk, A., Hare, A. A., Crabeck, O., Else, B. G. T., Campbell, K., Sørensen, L. L.,

943   Sievers, J., Papakyriakou, T. : Temporal dynamics of ikaite in experimental sea ice, The
944   Cryosphere, 8(4), 1469–1478, doi:10.5194/tc-8-1469, 2014.

945

946   Semiletov, I.P., Makshtas, A., Akasofu, S. I., and Andreas, E.L.: Atmospheric CO_2 balance:
947   The role of Arctic sea ice, Geophys. Res. Lett., 31, L05121, doi:10.1029/2003GL017996,
948   2004.

949

950   Sezgin, M., and Sankur . B.: Survey over image thresholding techniques and quantitative
951   performance evaluation, J. Electron. Imaging, 13, 146– 165, doi:10.1117/1.1631315,2004.

952

953   Shannon, C. E., and Weaver. W.: The mathematical theory of communication, Bell Syst.
954   Tech. J., 27, 379–423,1948.

955

956   Skoog, D. A., West, D. M. and Holler F. J.: Chimie Analytique, De Boeck Univ., Paris,1997.

957

958   Stefels, J., G. Carnat, J. W. H. Dacey, T. Goossens, J. T. M. Elzenga, and J. L. Tison. :The
959   analysis of dimethylsulfide and dimethylsulfoniopropionate in sea ice: Dry-crushing and
960   melting using stableisotope additions, Mar. Chem., 128–129, 34–43, 2012.

961

962   Timco, G. W., and Frederking. R. M. W.: A review of sea ice density, Cold Regions Science
963   and Technology, 24, 1-6,1996.

964

965   Tison, J. L., Haas, C., Gowing, M. M., Sleewaegen, S., and Bernard, A.: Tank study of
966   physico-chemical controls on gas content and composition during growth of young sea ice,
967   Journal of Glaciology, 48, 177-191, 2002.

968

969   Tsai, D. M. :A fast thresholding selection procedure for multimodal and unimodal histograms,
970   Pattern Recognition Lett., 16, 653 − 666, doi:10.1016/0167-8655(95)80011-H, 1995.

971

972   Tsurikov, V. :The formation and composition of the gas content of sea ice, J Glaciol, 22(86),
973   67-81,1979.

974

975   UNESCO. : Eight report of the joint panel on oceanographic tables and standards, UNESCO
976   Tech. Pap. Mar. Sci., 28 pp.,1978.

977

978 Vancoppenolle M, Meiners KM, Michel C, Bopp L, Brabant F, Carnat G, Delille B, Lannuzel

979 D, Madec G, Moreau S, Tison J-L, van der Merwe P. : Role of sea ice in global

980 biogeochemical cycles: Emerging views and challenges, Quaternary Science Reviews,

981 79:207-230, doi:10.1016/j.quascirev.2013.04.011,2013.

982

983 Worster, M. G.:The dynamics of mushy layers, in Interactive Dynamics of Convection and

984 Solidification, NATO ASI Ser. E219, pp. 113-138, Dordrecht : Kluwer, 1992.

985

986 Worster, M. G.: Convection in mushy layers, Annual Review of Fluid Mechanics, 29, 91-

987 122,1997.

988

989 Yen, J.-C., Chang, F. J. and Chang, S.:A new criterion for automatic multilevel thresholding,

990 IEEC Trans. Image Process., 4, 370 – 378, doi:10.1109/83.366472,1995.

991

992 Zack, G. W., Rogers, W. E. and Latt. S. A.: Automatic measurement of a sister chromatid

993 exchange frequency, J. Histochem. Cytochem., 25, 741– 753.1997.

994

995 Zemmelink, H. J., Delille, B., Tison, J. L., Hintsa, E. J., Houghton, L., and Dacey, J. W. H.:

996 CO_2 deposition over the multi-year ice of the western Weddell Sea, Geophysical Research

997 Letters, 33,L13606, doi:10.1029/2006GL026320, 2006.

998

999 Zhou, J. Y., Delille, B., Eicken, H., Vancoppenolle, M., Brabant, F., Carnat, G., Geilfus, N.

1000 X., Papakyriakou, T., Heinesch, B., and Tison, J. L.: Physical and biogeochemical properties

1001 in landfast sea ice (Barrow, Alaska): Insights on brine and gas dynamics across seasons,

1002 Journal of Geophysical Research-Oceans, 118, 3172-3189, 10.1002/jgrc.20232, 2013.

Table Captions

Temperature (°C)	Salinity	Length (cm)	Ice cube volume (cm3)	Masse (g)	Density (g cm3)	V_b (%)	V_a (%)
-5.00	5.00	4.93	119.82	113.75	0.95	5.1	-1.3
-5.00	5.00	5.00	125	113.75	0.91	4.9	2
-5.00	5.00	5.07	130.32	113.75	0.87	4.7	6.3
Relative standard error		±1.4%	±4.2%		±4.4%	±4.1%	±163%

Table 1. Effect of dimensional error on brine volume and air volume fraction computed by mass-volume density measurement using state equation from Cox and Weeks (1983).

$V_{air} = 50\%$	V_{air} x Hu_{air}	$0\% < V_{ice} < 50\%$	V_{ice} x Hu_{ice}	$0\% < V_{brine} < 50\%$	V_{brine} x Hu_{brine}	Hu value*
0.5	-500	0	0	0.5	100	-400
0.5	-500	0.1	-7.4	0.4	80	-427.4
0.5	-500	0.2	-14.8	0.3	60	-454.8
0.5	-500	0.3	-22.2	0.2	40	-482.2
0.5	-500	0.4	-29.6	0.1	20	-509.6
0.5	-500	0.5	-37	0	0	-577

$$*Hu = (V_{air} \times Hu_{air}) + (V_{ice} \times Hu_{ice}) + (V_{brine} \times Hu_{brine})$$

Table 2. Estimation of the Hu-value of a pixel containing at least 50 % of air. Assuming the Hu-value of air, of ice and brine are -1000, -74 and 200, respectively.

Data		January 14	January 16	January 25
Ice thickness (cm)		4	8	22
Temperature (C°)		-4.1—1.7	-8.4—1.6	-5.2--2.1
Salinity		11.4-25.8	2.26-10.3	1.3-12.5
Brine volume fraction (%) (V_b, liquid porosity)		11.8-58.6	2.26-20.4	1.3-20.6
Bulk ice Density (g cm^3)		0.91	0.89-0.92	0.84-0.92
Air volume fraction (%)(V_a, CT-derived air porosity)	Granular	0.69-5.09	1.8-10	0.69-19.41
	Columnar impermeable	Na	0.13-1.89	0.42-3.01
	Columnar permeable	0.18-1.25*	0.02-0.87	0.11-0.85
Air inclusions diameter (mm)	Granular	0.097-4.53	0.097-13.31	0.97-18.2
	Columnar impermeable	Na	0.097-4.86	0.097-4..96
	Columnar permeable	0.097-1.12	0.097-1.08	0.097-1.18
Gas composition (average mixing ratio)	O_2 %	23.7	29.4	27.24
	Ar %	1.4	2.2	1.96
	N_2 %	74.9	68.4	70.8
Buk ice total gas content (ml L^{-1} ice, O_2+Ar+N_2)		1.58	2.5-4.7	2-6.5
Gas Saturation factor (SAT_f)		0.82	9.5 (top) -1.2 (bottom)	16 (top)-0.9 (bottom)

* 98% of the air volume fraction recorded was under 1 %.
Table 3. Summarizes the main sea ice characteristics and sea ice properties

Air inclusion Classification	Abundance (% of the total Nbr of air inclusions observed)	Contribution (% of the air volume fraction produced by the air inclusion)	Location
Micro	78%	29%	Columnar and Granular
Large	20.7%	47%	Columnar and Granular (Depends most likely of V_b)
Macro	1.3%	24%	Granular/snow ice

Table 4. Classification and properties of the air inclusions. The "abundance" is the proportion of micro, large and macro bubble on the total number of air inclusions observed (100% is the total number of inclusions in the three datasets (Jan 14 + Jan 16 + Jan 25)). The "contribution" is the percentile of the porosity produced by the micro, large and macro inclusions (100% is the total of air volume fraction observed in the three data set (Jan 14+ Jan 16 +Jan 25)).

Data		January 14	January 16	January 25
Granular	**Permeability**	Permeable V_b=11%	Permeable V_b=6.2%	Permeable 3.9%<V_b<12%
	Saturation	Na	Supersaturated SAT_f=9.5	Supersaturated SAT_f=16
	Air volume fraction	0.74%-5.09%	1.8%-10%	0.69%-19.41%
	Bubble class	Micro and large	Micro, large and macro	Micro, large and macro
Intermediate columnar	**Permeability**	Na	Impermeable	Impermeable
	Saturation	Na	Supersaturated	Supersaturated
	Air volume fraction	Na	V_a<2%	V_a<2%
	Bubble class	Na	Micro and large	Micro and large
Bottom columnar	**Permeability**	Permeable	Permeable	Permeable
	Saturation	Subsaturated SATf≤1.2	Subsaturated SATf≤1.2	Subsaturated SATf≤1.2
	Air volume fraction	Va<1%	Va<1%	Va<1%
	Bubble class	90 % Micro	90 % Micro	90% Micro

Table 5. Physical characteristics of the various ice types. Where the brine volume exceeds the permeability threshold for columnar ice of 5% V_b (Golden et al., 1998,2007), the ice layer is so-called permeable.

1071

Nucleation Processes	Limitation factor	Abundance (% of the total Nbr of air inclusions observed)	Contribution (% of porosity produced by the inclusions)	Type of air inclusions produced	Location
Convection driven	Saturation level	14%	8.4%	Most likely micro	subsaturated columnar
Solubility Driven	Brine volume fraction	60%	44%	Micro to large	Supersaturated Columnar
Snow ice formation		26%	47%	Micro Large Macro	Granular/ snow ice

1072
1073 **Table 6.** Main parameters influencing the air volume fraction. The "abundance" is the
1074 proportion of the inclusions concerned by the processes on the total of inclusion observed
1075 (100% is the total of inclusions observed in the three data set (Jan 14+ Jan 16 +Jan 25)). The
1076 "contribution" is the percentile of the porosity produced by the inclusions formed by
1077 convection driven, solubility driven and snow ice formation processes, respectively (100% is
1078 the total of air volume fraction observed in the three data set (Jan 14+ Jan 16 +Jan 25)).
1079
1080

Fig.Captions
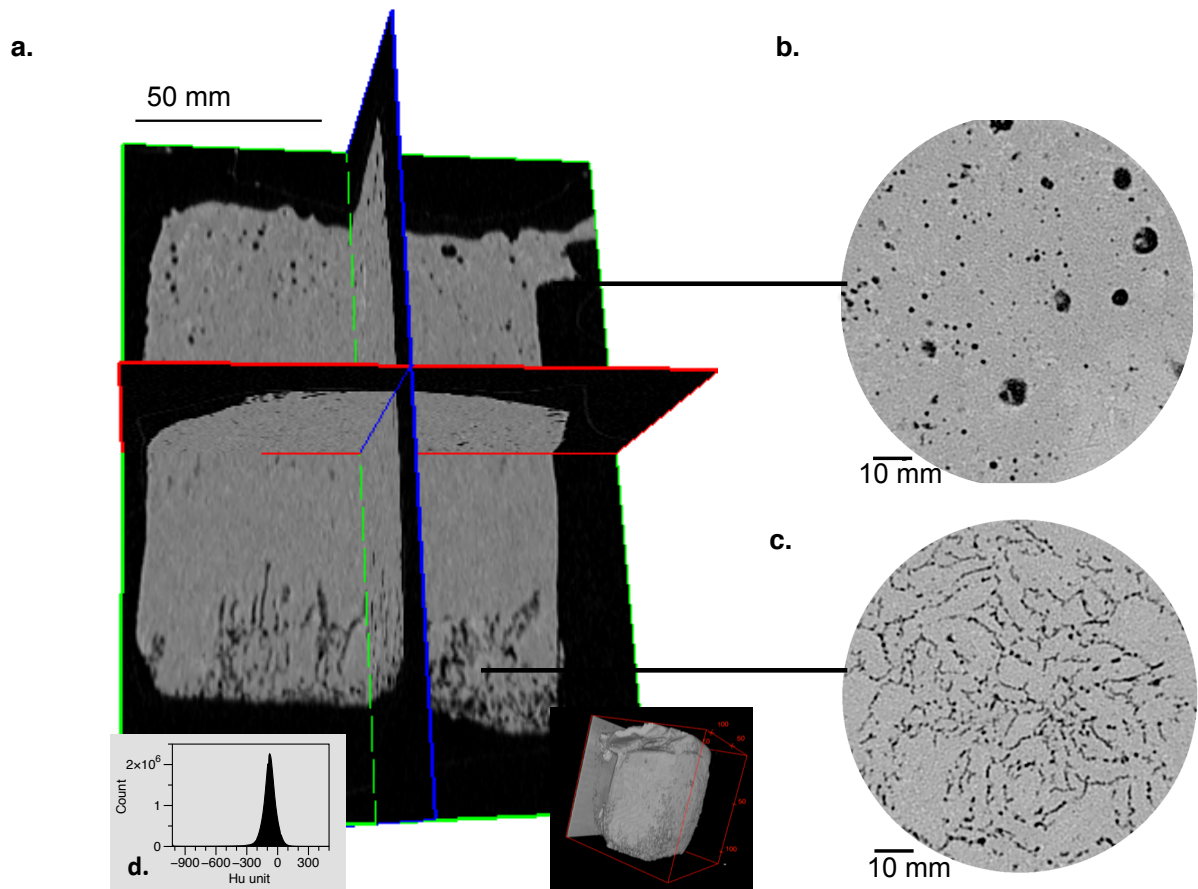
1083   **Figure.1 (a)** 3D Orthoslice view from raw images of January 16, consisting of two
1084   longitudinal slices and one transversal slice, lighter grey represent the ice matrices and black
1085   area represent the air inclusions (i.e bubbles); **(b)** Top Transversal slice at 0.65 mm depth,
1086   every black dot represents an air inclusion (i.e bubbles); **(c)** Bottom transversal slice at 8 cm
1087   depth, all the black dots show drained brine ; panel (d) Histogram of HU-unit (Ct-value)
1088   recorded for 186 transversal slices of 0.6 mm thick for January 16.
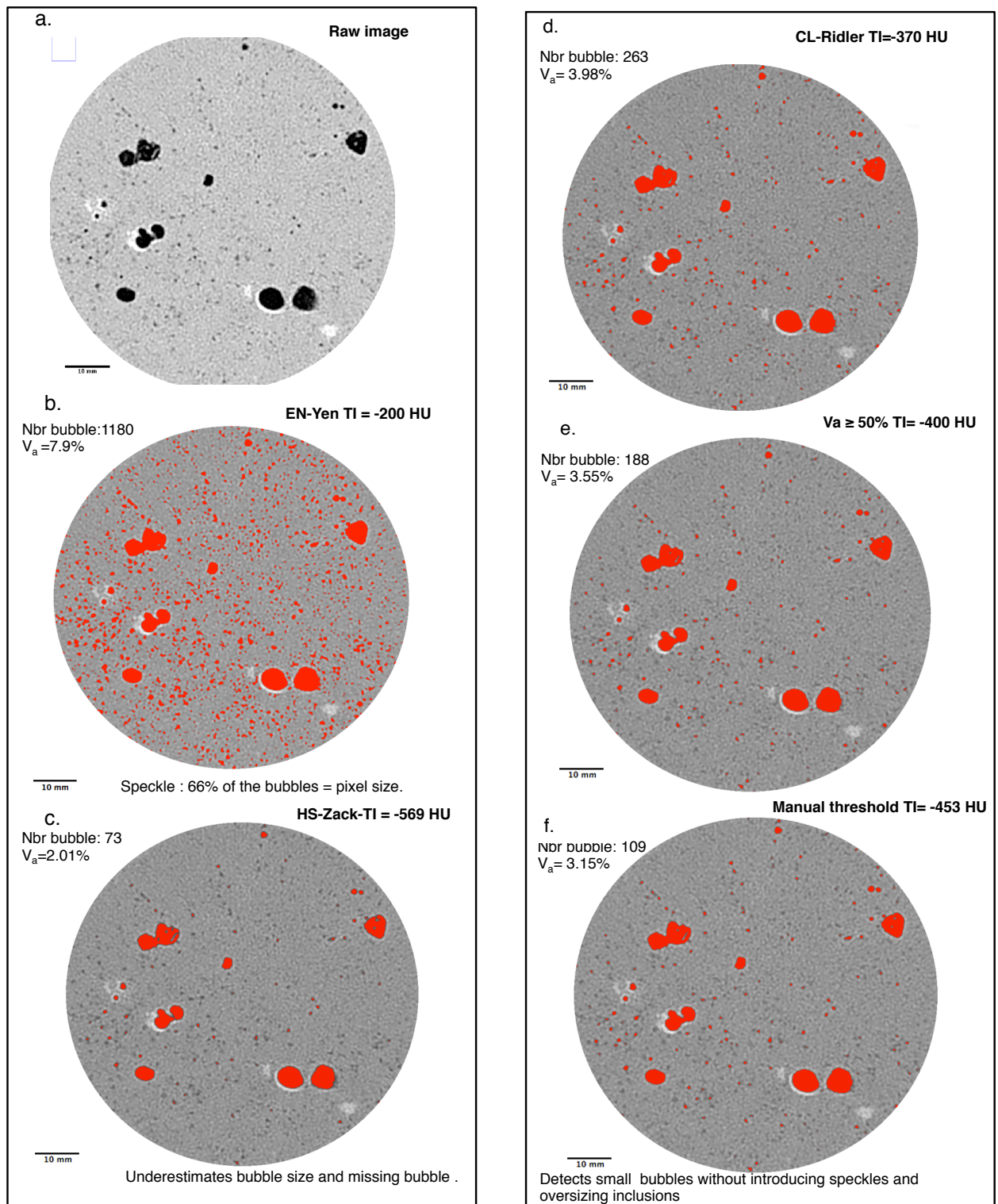
Figure 2. (a) Raw transversal slice where grey pixels represent ice, black pixels represent air, and darker grey pixels are pixel-containing air. **(b)** and **(c)** Transversal slices showing the air selected pixels in red using a HU-value of -200 and of -569 as threshold selected by the EN-Yen **(b)** and the HS-Zack algorithm **(c),** respectively. **(d), (e)** and **(f)** Transversal slices showing the air selected pixels in red using a HU-value of -370, of -400 and of -453 as threshold selected by **(d)** CL-Ridler algorithm, **(e)** by pixels containing a minimum of 50% of air and **(f)** by manual thresholding.
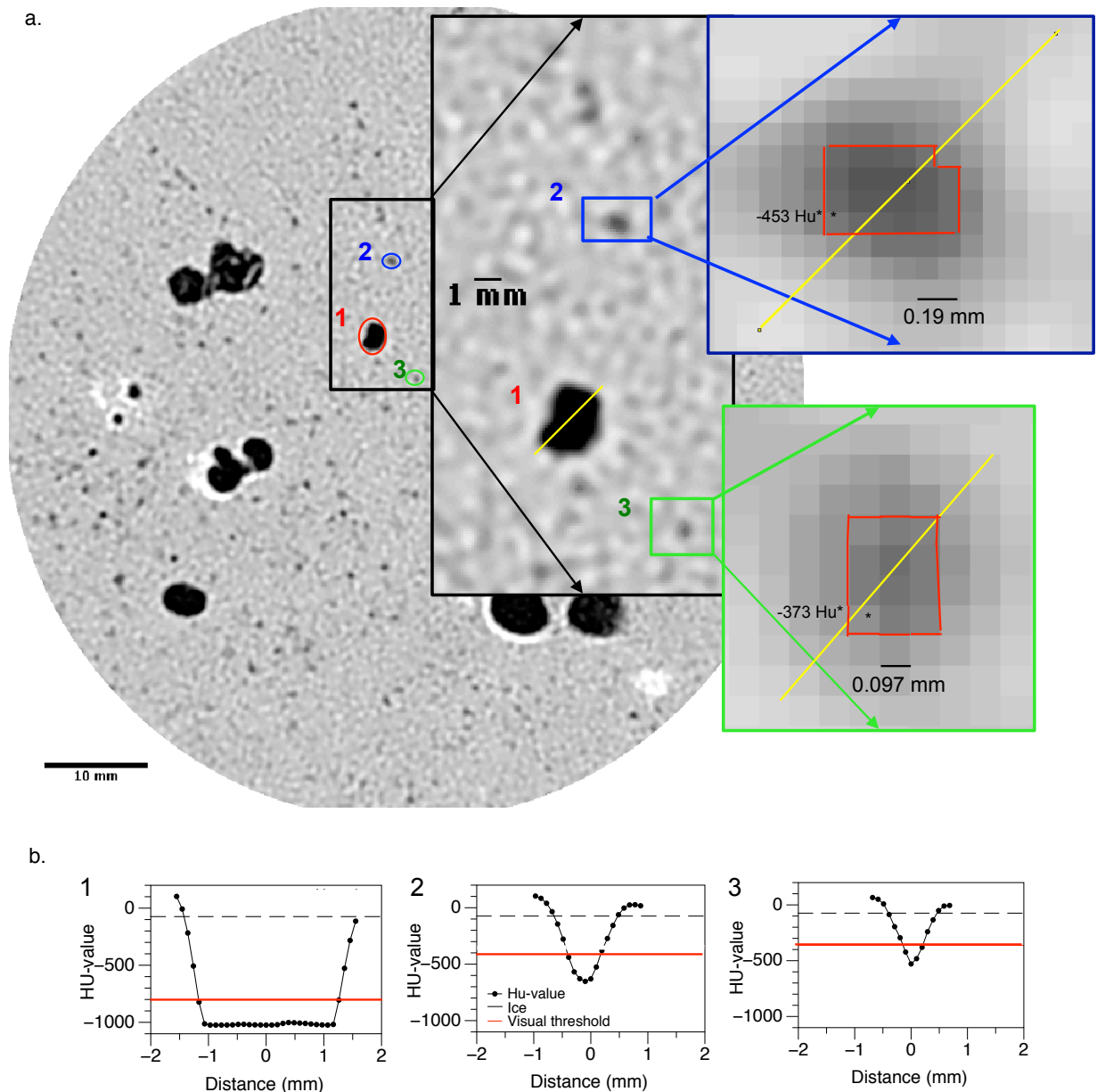
Figure 3. (a) Raw transversal slice where grey pixels represent ice and black pixels represent air, darker grey pixels are pixels containing air and white pixels are containing brine. We highlighted three air inclusions: an air inclusion (1) larger than the spatial resolution and two inclusions (2 and 3) which are smaller than the spatial resolution, their Hu-value never reached the Hu –value of air, instead there appeared as mixed pixels and their Hu-value reflects the proportion of air, ice and brine in the pixel. The red line shows the visual boundary of the bubble where the lowest Hu-value observed for pixel (*) is the visual threshold. **(b)** The distribution of HU-value along the transects (yellow lines in panel a).
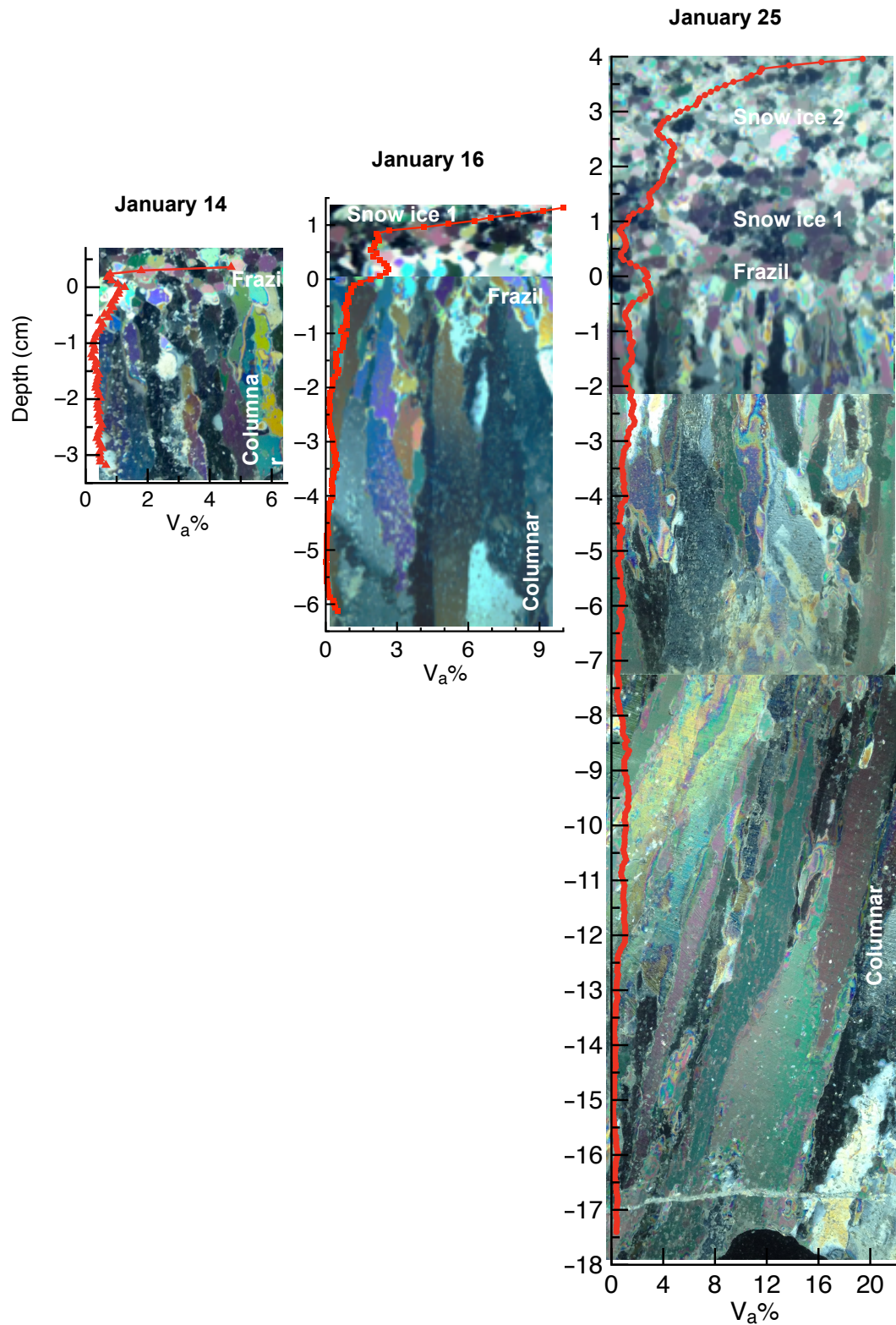
Figure 4. Sea ice microstructural images overlain by the air volume fraction (red curve) for January 14, 16 and 25. The x scale differs for each date in order to visualize vertical change. The zero depth is fixed at the boundary between granular and columnar ice. Through the studied period ice grew from the bottom increasing the columnar layer, as well as by the top due to additional formation of snow ice.
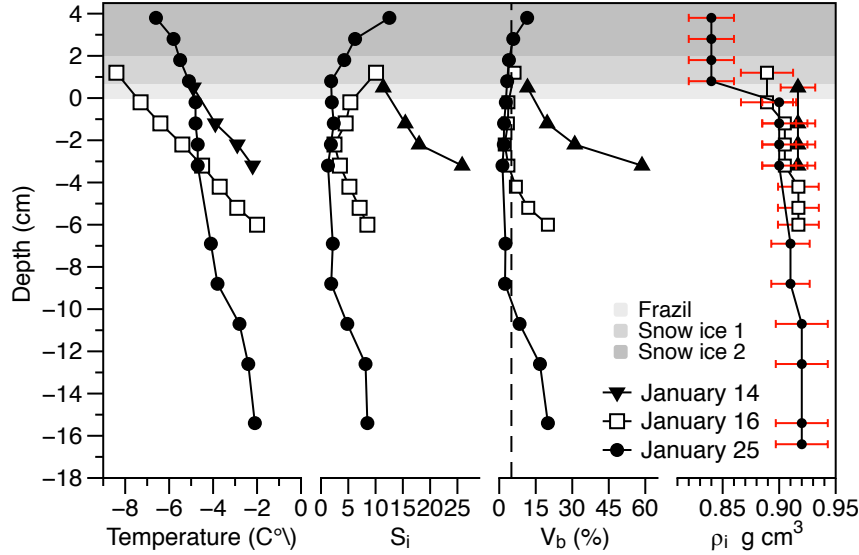
Figure 5. Ice in situ temperature (°C), bulk ice salinity, and brine volume fraction (V_b) and bulk ice density profiles (g cm^{-3}) on 14, 16, 25 Jan. The dotted line at 5% on the V_b panel refers to the theoretical liquid permeability threshold for columnar sea ice (Golden et al. 1998). Red bars on the density profiles indicate the standard deviation of the mean of density measurements derived from the mass-volume technique.
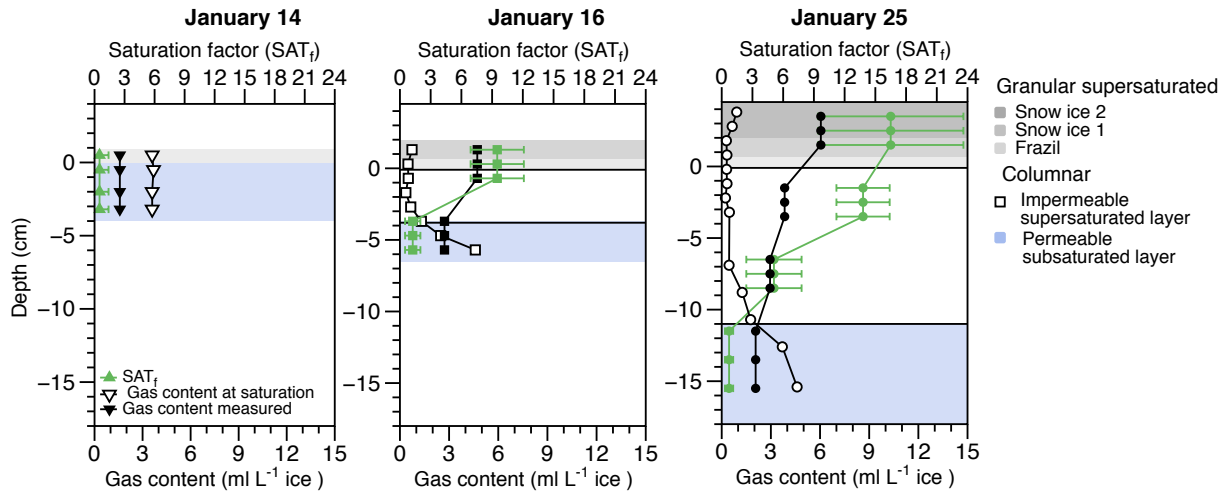
Figure 6. Profiles of the total gas content in bulk sea ice measured by gas chromatography as the sum of O_2, N_2 and Ar (black symbols) compared (i) to the theoretical bulk ice gas content at atmospheric saturation (white symbols) and (ii) the saturation factor (green symbols). The blue area highlights subsaturated columnar sea ice (SAT$_f$ ≤1.2), the white area highlights the supersaturated columnar sea ice (SAT$_f$ >1.2) and the grey area represents successively the supersaturated granular layers (frazil and snow ice layers).
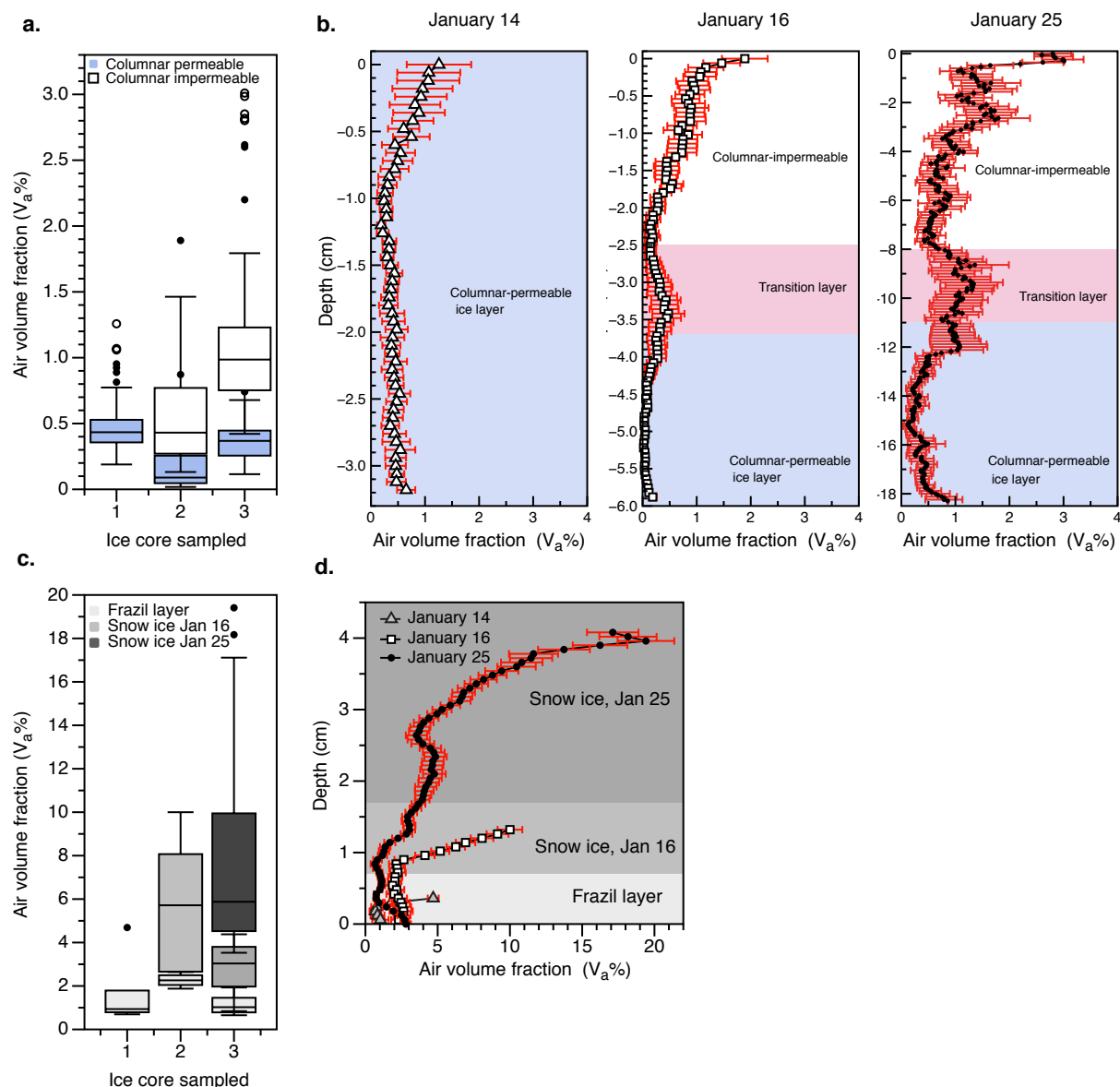
Figure 7. (a) IQR box plot showing the distribution of CT-derived V_a computed for every 0.6 mm thick slice of each ice core in the the columnar impermeable and bottom columnar permeable layers on January 14 (1), 16 (2) and 25 (3), respectively. The box is defined by the first and third quartiles of the distribution, the line in the box is the median, the circles represent the outliners (an outlier is any value that lies more than one and a half times the length of the box from either end of the box, T-bars). **(b)** V_a profile in the columnar layers for January 14, 16 and 25, respectively. The Y scale differs for each date to obtain better visualisation of the V_a profile. The errors bars show the potential range of CT-derived V_a in each transverse slice. **(c)** IQR box plot showing the distribution of CT-derived V_a computed for every 0.6 mm thick slice of each ice core in granular layers and **(d)** V_a profile in granular ice for each sampling date.
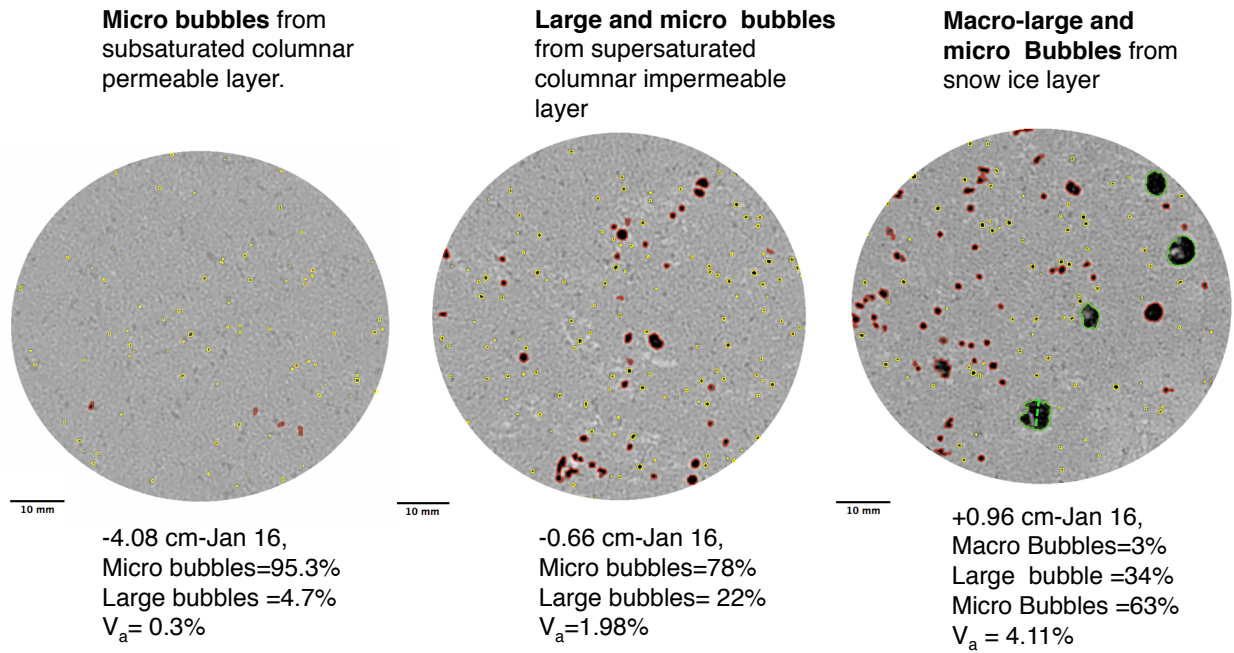
Micro bubbles from subsaturated columnar permeable layer.

Large and micro bubbles from supersaturated columnar impermeable layer

Macro-large and micro Bubbles from snow ice layer

-4.08 cm-Jan 16,
Micro bubbles=95.3%
Large bubbles =4.7%
V_a= 0.3%

-0.66 cm-Jan 16,
Micro bubbles=78%
Large bubbles= 22%
V_a=1.98%

+0.96 cm-Jan 16,
Macro Bubbles=3%
Large bubble =34%
Micro Bubbles =63%
V_a = 4.11%

Figure 8. Transversal slice at different depth highlighting the proportion of micro (yellow), large (red) and macro (green) bubble in each slice (e.g. [Nbr micro /(Nbr micro+NbrLarge +Nbr Macro)]x100).
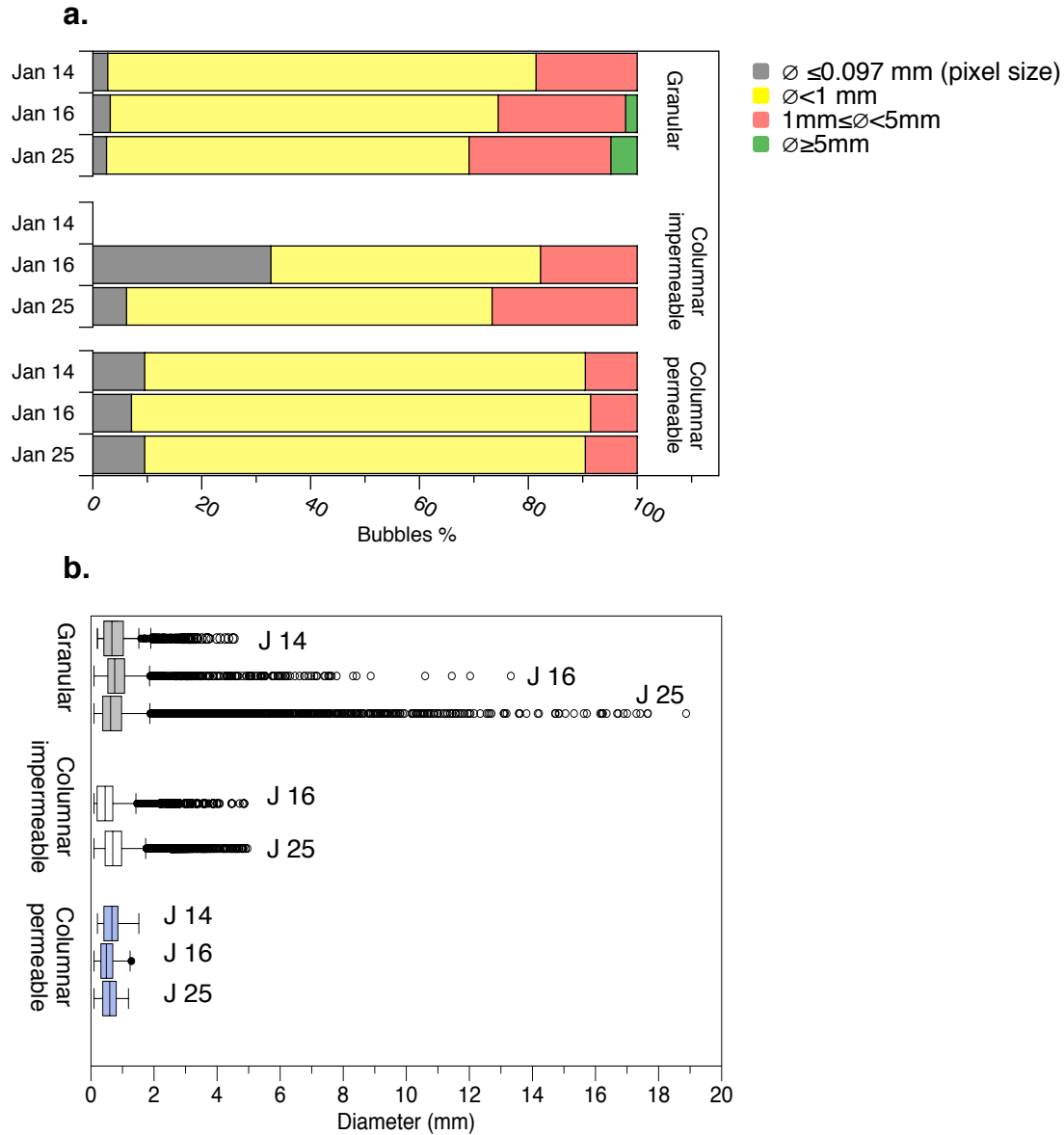
Figure 9. (a) The proportion of micro, large and macro bubbles for each ice type and sampling date. **(b)** IQR box plot showing the distribution of the bubble diameters, per ice type and sampling dates. The box is defined by the first and third quartiles of the distribution, the line in the box is the median, the circles represent the outliners (an outlier is any value that lies more than one and a half times the length of the box from either end of the box, T-bars)
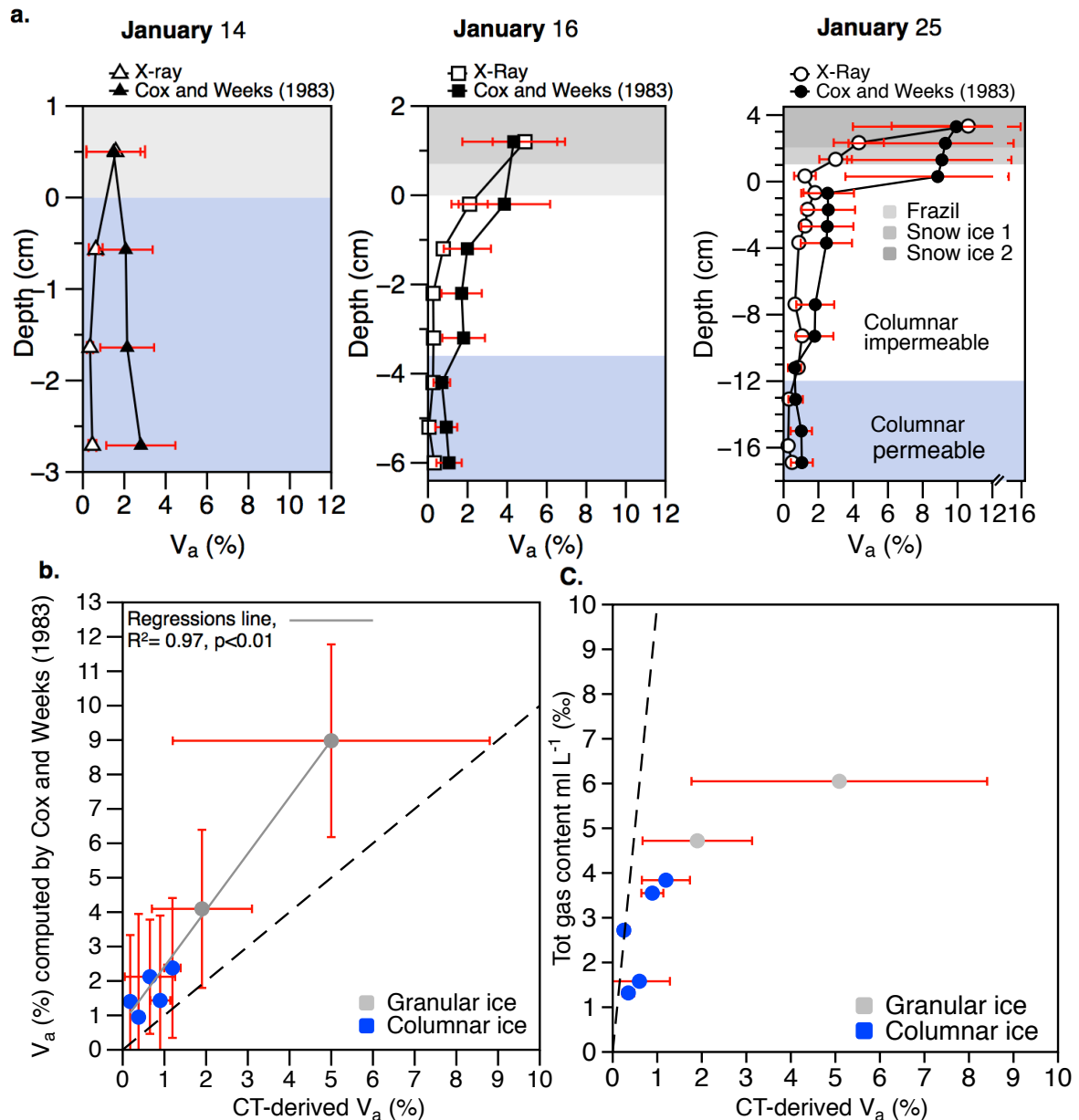
Figure 10. (a) Air volume fraction profiles derived from the Cox and Weeks (1983) equations (filled black symbols) using density measurements, with error bars showing the standard deviation from the mean of the results. These are compared to the CT-derived air volume fraction averaged for 2 cm section (filled white symbols) which error bars show the standard deviation of the mean along the 2 cm section. **(b)** The relationship between CT-derived air volume fraction and the Cox and Weeks (1983) air volume fraction where the dotted line signifies the 1:1 relationship. **(c)** The relationship between CT-derived air volume and the GC-derived bulk ice total gas content measured where the dotted line signifies the 1:1 relationship. In (b) and (c) the CT-derived air volume fractions are averaged for 5 cm section and error bars show the standard deviation of the mean along the 5 cm section. Where CT-derived air volume fraction spans a large range of values along the section (e.g. granular ice), the standard deviation of CT-derived air volume fraction increases.
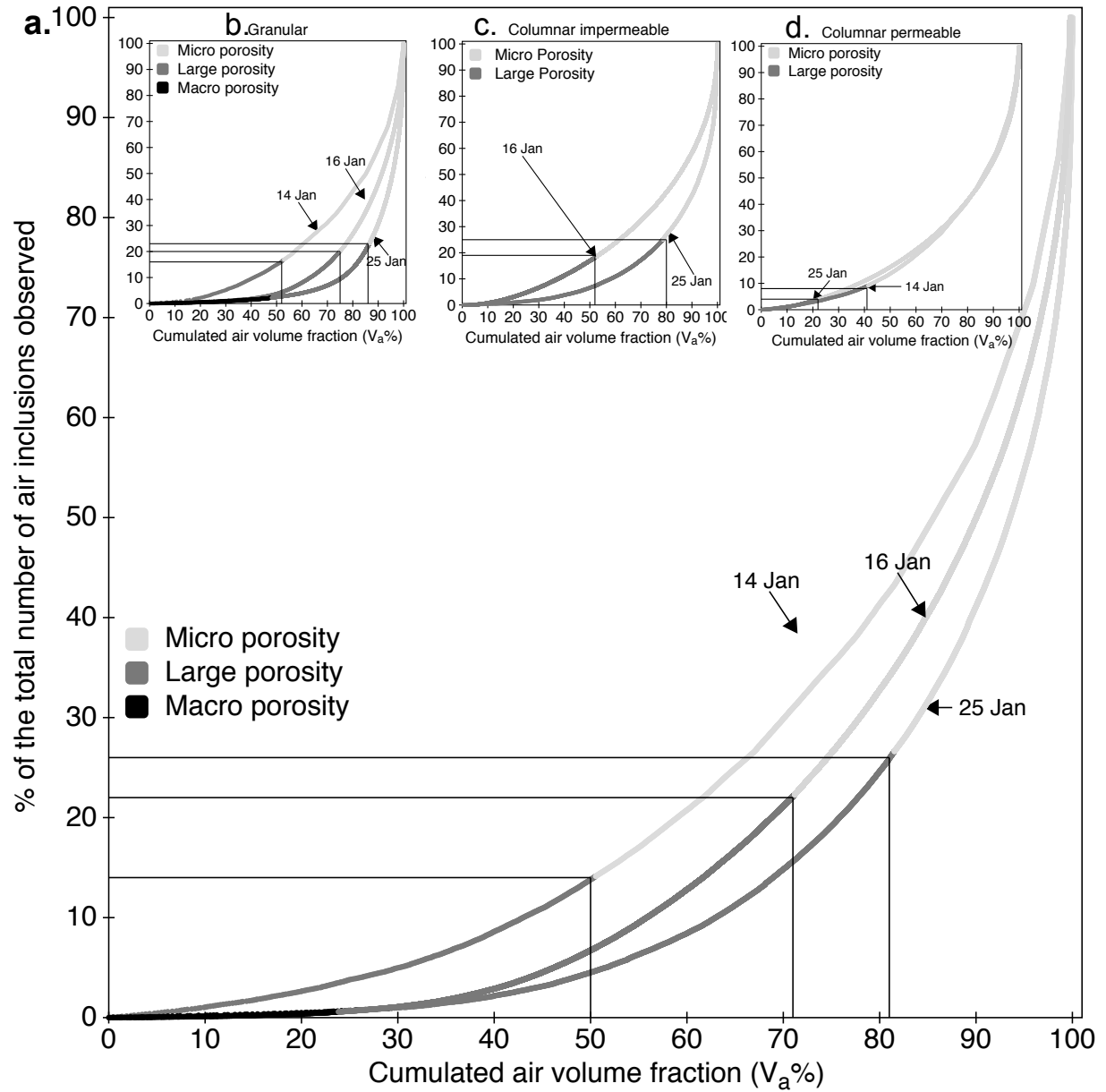
1169

Figure 11. The cumulated contribution of the macro, large and micro bubbles to the cumulated relative air volume fraction for the whole ice core **(a)**, and in granular **(b)**, columnar impermeable **(c)** and columnar permeable ice **(d).** It shows that, a smaller number of large bubbles (e.g. Large on 25 Jan) produced most of the air volume fraction (i.e porosity), and this is true for both the whole ice core (a) and for each type of ice (b, c, d).
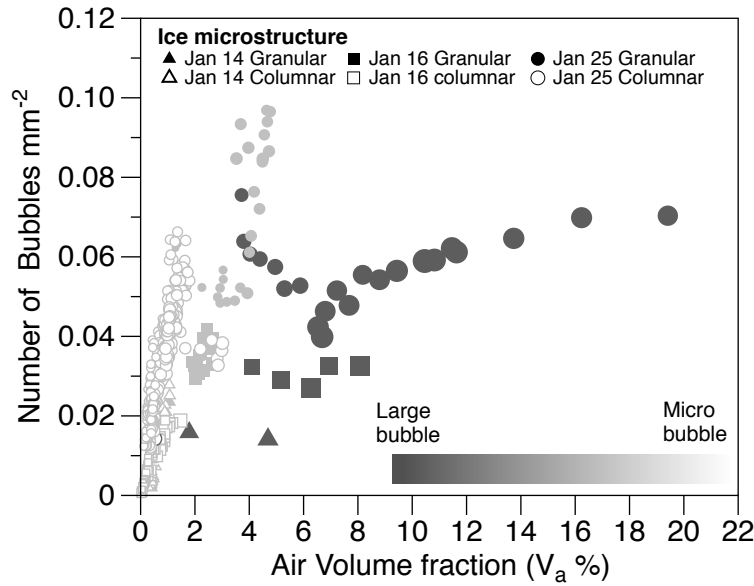
Figure 12. The relationship between bubble density: number of bubbles per mm^{-2} (slice area) and air volume fraction per slice as a function of both bubble size class and ice type (granular and columnar crystal texture).
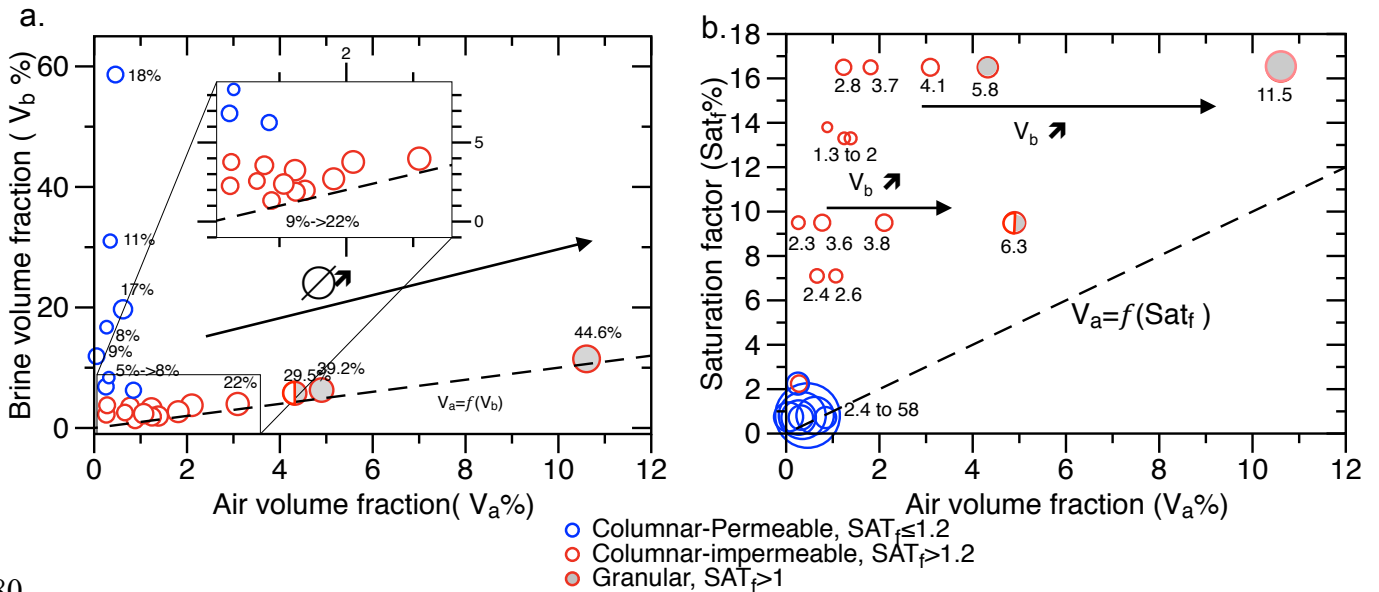

Figure 13. (a) Relationship between brine volume fraction and air volume fraction as a function of the bubble size (where the size of each marker circle is proportional to the percentage of bubbles with diameters >1mm, written as % value next to some of circles). **(b)** Relationship between the air volume fraction and the saturation factor as a function of the brine volume fraction. The size of each circle denotes the brine volume fraction (%, written next to some of the circles). In each panel, the bottom columnar permeable subsaturated ice ($SAT_f \leq 1.2$, blue circles) is differentiated from the columnar impermeable supersaturated ice ($SAT_f > 1.2$, red circles), and from the top granular supersaturated ice ($SAT_f > 1.2$, grey circles).
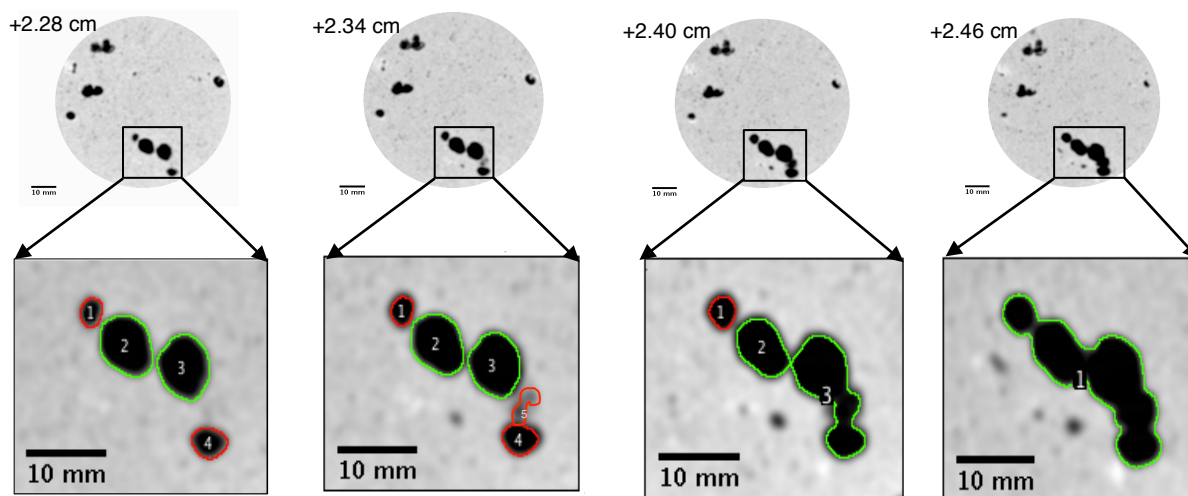
1190
1191
1192 **Figure 14**. Four successive slices in the snow ice layer on January 25 from +2.28 to +2.46
1193 cm below the surface. At 2.28cm, four individual bottom end of bubbles exist where at
1194 2.46cm, the top end of each bubbles are joined and formed a single bubble.
1195

1196